The Astronomical Journal, 131:168–184, 2006 January

DIFFUSE OPTICAL LIGHT IN GALAXY CLUSTERS. I. ABELL 3888

J. E. Krick and R. A. Bernstein

Astronomy Department, University of Michigan, Ann Arbor, MI 48109; jkrick@umich.edu, rabernst@umich.edu

and

K. A. Pimbblet

Department of Physics, University of Queensland, Brisbane, QLD 4072, Australia; pimbblet@physics.uq.edu.au

Received 2005 February 10; accepted 2005 September 18

ABSTRACT

We are undertaking a program to measure the characteristics of the intracluster light (ICL; total flux, profile, color, and substructure) in a sample of 10 galaxy clusters with a range of cluster mass, morphology, and redshift. We present here the methods and results for the first cluster in that sample, A3888. We have identified an ICL component in A3888 in V and r that contains 13% ± 5% of the total cluster light and extends to 700 h_{70}^{-1} kpc ($\sim 0.3 r_{200}$) from the center of the cluster. The ICL color in our smallest radial bin is $V - r = 0.3 \pm 0.1$, similar to the central cluster elliptical galaxies. The ICL is redder than the galaxies at 400 h_{70}^{-1} kpc $< r <$ 700 h_{70}^{-1} kpc, although the uncertainty in any one radial bin is high. Based on a comparison of $V - r$ color with simple stellar models, the ICL contains a component that formed more than 7 Gyr ago (at $z > 1$) with a high-metallicity ($1.0\ Z_{\odot} < Z_{\rm ICL} \lesssim 2.5\ Z_{\odot}$) and a more centralized component that contains stars formed within the past 5 Gyr (at $z \sim 1$). The profile of the ICL can be roughly fitted by a shallow exponential in the outer regions and a steeper exponential in the central region. We also find a concentration of diffuse light around a small group of galaxies 1.4 h_{70}^{-1} Mpc from the center of the cluster. In addition, we find three low surface brightness features near the cluster center that are blue ($V - r = 0.0$) and contain a total flux of $0.1 M_{*}$. Based on these observations and X-ray and galaxy morphology, we suggest that this cluster is entering a phase of significant merging of galaxy groups in the core, whereupon we expect the ICL fraction to grow significantly with the formation of a cD galaxy, as well as the infall of groups.

Key words: cosmology: observations — galaxies: clusters: individual (A3888) — galaxies: evolution — galaxies: interactions — galaxies: photometry

1. INTRODUCTION

Galaxy clusters contain a population of stars that are not members of individual galaxies but are bound to the cluster potential, producing diffuse intracluster light (ICL). This ICL component has been found in a number of clusters through surface brightness measurements and direct detections of resolved stars including planetary nebulae, red giants, supernovae (SNe), novae, and globular cluster systems. These investigations indicate that the optical ICL comprises between 5% and 50% of the total optical cluster luminosity (see Feldmeier et al. 2004; Gonzalez et al. 2005; Zibetti et al. 2005, and references therein). Conclusions on the color of the ICL vary widely from blue to red, with and without color gradients (Schombert 1988; Mackie 1992; Gonzalez et al. 2000; Zibetti et al. 2005). Current measurements of the shape of the ICL generally favor a double de Vaucouleurs profile such that one function fits the brightest cluster galaxy (BCG) and the second function fits the extended envelope (Gonzalez et al. 2000; Bernstein et al. 1995; Zibetti et al. 2005). Examples of tidal features such as plumes and bridges are found in multiple clusters as evidence of interactions that add stars to the ICL (Gregg & West 1998; Calcáneo-Roldán et al. 2000; Feldmeier et al. 2004). Long-slit spectroscopy of A2199 shows that the intracluster stars there have the same velocity dispersion as the cluster galaxies (Kelson et al. 2002), confirming that, in at least one cluster, the intracluster stars are not bound to the individual galaxies but trace the overall cluster potential. Conversely, intracluster planetary nebula studies show evidence for less relaxed velocities (Arnaboldi et al. 2004; Gerhard et al. 2005). There is no consensus on the velocity distribution of intracluster stars.

The ICL is a fossil remnant of cluster formation and evolution and can be used to study the dominant physical processes involved in galaxy evolution in clusters. Hierarchical dark matter simulations suggest that galaxies falling into dense regions would lose most of their mass. When mechanisms such as radiative cooling and star formation are included in the simulations, galaxies composed of a central dense core of stars retain most of their stellar mass throughout cluster infall but lose some stars to the cluster potential. State-of-the-art simulations are able to predict the existence of this intracluster population, but basic questions as to its properties can only be answered by understanding which physical mechanisms are important. This work seeks to discover when and how intracluster stars are formed by studying the total flux, profile shape, color, and substructure in the ICL as a function of cluster mass, morphology, and redshift.

Observations of the total flux in the ICL over a sample of clusters will allow us to identify the effects of cluster environment on galaxy evolution. For example, a high-mass cluster should have a higher ICL fraction than low-mass clusters if ram pressure stripping or harassment are dominant mechanisms. In fact, simulations by both Lin & Mohr (2004) and Murante et al. (2004) predict a strong relation between ICL fraction and mass. If, however, galaxy-galaxy merging is the dominant mechanism and most of the galaxy evolution happens early on in cluster collapse, then the ICL should not correlate directly with current cluster mass. The existence of a cD galaxy in a cluster is evidence of a rich merger history, and therefore, morphology should also correlate strongly with ICL fraction. The ICL fraction will be affected by redshift, since with time comes an increased number of interactions.

Observations of the color and substructure of the ICL will help identify the origin, formation epoch, metallicity, and possibly

progenitor morphologies of cluster galaxies. For example, if the ICL is as red or redder than the bright cluster elliptical galaxies, it is likely to be a remnant from the early epochs of cluster formation with little recent accretion of tidally disrupted systems. If the ICL is bluer than the galaxies, then some recent accretion has occurred, either from elliptical galaxies with low metallicity or spiral galaxies with younger stellar populations. While multiple mechanisms are likely to play a role in the complicated process of the formation and evolution of clusters, important constraints can come from ICL measurement in clusters with a wide range of properties.

In addition to constraining galaxy evolution, the ICL is an important baryonic component in clusters. The ICL, which is typically not included in the baryon census, will contribute to the baryon fraction of clusters, and that contribution is likely to change with time. If the ICL fraction does indeed evolve with redshift and is a significant fraction of the total cluster light, it will systematically bias the inferred redshift dependence of the baryon fraction. Recent work by Allen et al. (2004) has used a change in baryon fraction with redshift of only a few percent to constrain cosmological parameters. When doing such precision cosmology it will be necessary to include ICL in the cluster light budget.

The ICL may also play an important role in the global properties of the intracluster medium (ICM). It has recently been suggested that an intracluster stellar population (ICSP) can account for at least some amount of heating and metal enrichment of the ICM (Zaritsky et al. 2004; Lin & Mohr 2004; Domainko et al. 2004). Considering only SNe *within* galaxies, the full metallicity of the ICM cannot easily be accounted for (Lin & Mohr 2004). However, since intracluster SNe are in situ in the ICM, they contribute directly to the metallicity of the ICM and will therefore have a direct impact on its abundance. Although these authors find that the ICL cannot fully account for the high abundance of the ICM ($\sim 0.3\ Z_{\odot}$), further studies are warranted to quantify just how many intracluster SNe there are. Even if the ICSP cannot account for the full metallicity of the ICM, it is possible that this population is responsible for the metallicity gradient found in clusters. If true, a correlation between ICL flux and abundance gradients in clusters should exist.

In this paper we present the methods of this survey, as well as measurements of the color, total flux, and profile shape for the first cluster in our sample, A3888. In § 2 we discuss the characteristics of the entire sample. Details of the observations and reduction are presented in §§ 3 and 4, including flat-fielding and sky background–subtraction methods. In § 5 we discuss object detection and removal, as well as cluster membership. In § 6 we describe our results, followed by a discussion of accuracy limits in § 7. In § 8 we present a discussion of the results. Conclusions are summarized in § 9.

Throughout this paper we use $H_0 = 70$ km s^{-1} Mpc^{-1}, $\Omega_M = 0.3$, and $\Omega_\Lambda = 0.7$, which gives 3.5 kpc arcsec^{-1} at the distance of A3888.

2. THE SAMPLE

The 10 galaxy clusters in our survey were selected to meet two general criteria. First, each cluster has a published X-ray luminosity that guarantees the presence of a cluster and provides an estimate of the cluster's mass. Second, all are at high Galactic and ecliptic latitude along lines of sight with low H I column density. This minimizes complications due to scattered light from Galactic stars and zodiacal dust and from variable extinction across the cluster field. Of the clusters that meet the above qualifications, we selected 10 clusters as the beginning of a statistical sample representative of a wide range in cluster characteristics, namely, redshift, morphology, spatial projected density (richness), and X-ray luminosity (mass).

To the extent possible, we also selected clusters for which mass estimates and membership information are available in the literature. For example, in addition to published X-ray masses, three of the clusters have mass estimates from gravitational lensing measurements. Published redshift surveys provide velocity dispersions and membership information for all but two clusters in the survey. Those two clusters, as well as five others with small numbers of published velocities, were included in a redshift survey we undertook with IMACS on Magellan I (Baade). With these additional observations the physical properties of all clusters in our sample can be compared to the ICL characteristics. Table 1 lists the relevant information for the cluster sample.

The sample is divided into a "low" ($0.05 < z < 0.1$) and a "high" ($0.15 < z < 0.3$) redshift range observed with the 1 m Swope and 2.5 m Du Pont telescopes, respectively. The bottom end of the redshift range is limited by the field of view of the 1 m telescope and detector, which corresponds to $0.9\ h_{70}^{-1}$ Mpc $\times$ $1.4\ h_{70}^{-1}$ Mpc ($14\farcm8 \times 22\farcm8$) at $z = 0.05$. This field of view allows us to measure the ICL, as well as off-cluster background flux in the same image for all clusters in the sample. The top end of the redshift range reflects X-ray data availability and the increasing difficulty of measuring diffuse sources at high redshift due to $(1 + z)^4$ surface brightness dimming.

2.1. *A3888*

This paper focuses on one cluster in our sample, A3888, which is a richness class 2 cluster at $z = 0.15$ (Abell et al. 1989). This Bautz-Morgan (B/M) type I-II cluster has no cD galaxy; instead, the core comprises three distinct subclumps of multiple galaxies each. At least two galaxies in each of these clumps are confirmed members (Teague et al. 1990; Pimbblet et al. 2002). On large scales (286, 535, and 714 h_{70}^{-1} kpc) Girardi et al. (1997) find a unimodal distribution for this cluster, with no detected substructures in either the galaxy spatial or velocity distribution. The projected spatial distribution of galaxies in A3888 is slightly elongated, with an ellipticity of 0.43 (Struble & Ftaclas 1994). X-ray surface brightnesses obtained from *XMM-Newton* observations also indicate an elongated, single-peaked distribution for the hot gas. The cluster contains an X-ray-bright Seyfert I galaxy located at a projected distance of roughly 600 h_{70}^{-1} kpc from the cluster center (Reimers et al. 1996).

The mass of A3888 can be estimated from two different sets of observations. Reiprich & Böhringer (2002) calculate gravitational mass based on pointed *ROSAT* PSPC count rates and the *ROSAT-ASCA* L_X-T_X relation (Markevitch 1998). Assuming an isothermal distribution and employing hydrostatic equilibrium, they find $M_{200} = 25.5^{+10.8}_{-7.4} \times 10^{14}\ h_{70}^{-1}\ M_{\odot}$, where $r_{200} = 2.8\ h_{70}^{-1}$ Mpc, which is defined as the radius within which the mean mass density is equal to 200 times the critical density. In a complementary method, mass can be determined from published galaxy velocity dispersions. Based on redshifts for 50 member galaxies located within a radius of $3.11\ h_{70}^{-1}$ Mpc (Teague et al. 1990) and using the method described by Girardi & Mezzetti (2001), we find that the mass of A3888 within r_{200} is $M_{200} = 40.2^{+10.6}_{-7.4} \times 10^{14}\ h_{70}^{-1}\ M_{\odot}$. For the purpose of this work, these two mass estimates are in good agreement, particularly since this cluster is elongated and likely not in dynamic equilibrium.

3. OBSERVATIONS

Observations for the entire sample of 10 clusters have been completed. The high-redshift observations were made with the du Pont

TABLE 1

CLUSTER CHARACTERISTICS

Cluster Name	R.A. (J2000.0)	Decl. (J2000.0)	l (deg)	b (deg)	z	B/M	Richness Class	L_X (10^{44} ergs s^{-1})	σ_v (km s^{-1})	No. of Confirmed Members	n(H I)[a] (10^{20} cm^{-2})	Lensing Measurement
A4059[b]	23 57	−34 40	356.8	−76.06	0.048[c]	I	1	3.09[a]	845^{+280}_{-140}[d]	45[e,f]	1.1	...
A3880[b]	22 28	−30 34	17.99	−58.50	0.058[c]	II	0	1.86[a]	827^{+120}_{-79}[g]	122[h,i,j]	1.1	...
A2734[b]	00 11	−28 52	19.46	−80.98	0.062[c]	III	1	2.55[a]	628^{+61}_{-57}[g]	127[k,f,j]	1.8	...
A2556[b]	23 13	−21 38	41.37	−66.97	0.087[c]	II-III	1	2.47[a]	1247^{+249}_{-249}[d]	5[l,m,n]	2.0	...
A4010[b]	23 31	−36 30	359.0	−70.60	0.096[c]	I-II	1	5.55[a]	625^{+127}_{-95}[g]	30[k,f]	1.4	...
A3888	22 34	−37 43	3.96	−59.40	0.151[c]	I-II	2	14.52[a]	1102^{+137}_{-107}[o]	69[p]	1.2	...
A3984[b]	23 15	−37 48	359.0	−67.19	0.181[c]	II-III	2	9.18[a]	...	...[i]	1.7	...
A0141[b]	01 06	−24 35	175.3	−85.93	0.23[c]	III	3	12.62[a]	...	...[q]	1.8	Dahle et al. (2002)
AC118	00 14	−30 2	8.90	−81.24	0.308[c]	III	3	22.05[a]	1947^{+292}_{-201}[r]	363[s,t,r]	1.7	Smail et al. (1991)
AC114	22 58	−34 47	8.32	−64.78	0.31[q]	II-III	2	12.7[u]	1388^{+128}_{-71}[o]	380[t,v,r]	2.0	Smail et al. (1991)

NOTE.—Units of right ascension are hours and minutes, and units of declination are degrees and arcminutes.

[a] From Ebeling et al. (1996).

[b] Clusters for which we have done a photometric and spectroscopic survey for additional membership information (see § 2).

[c] From Struble & Rood (1999).

[d] From Wu et al. (1999).

[e] From Chen et al. (1998).

[f] From Mazure et al. (1996).

[g] From Girardi et al. (1998).

[h] From Stein (1996).

[i] From Collins et al. (1995).

[j] From De Propris et al. (2002).

[k] From den Hartog (1995).

[l] From Ciardullo et al. (1985).

[m] From Kowalski et al. (1983).

[n] From Batuski et al. (1999).

[o] From Girardi & Mezzetti (2001).

[p] From Teague et al. (1990).

[q] From Abell et al. (1989).

[r] From Couch & Sharples (1987).

[s] From Busarello et al. (2002).

[t] From Couch & Newell (1984).

[u] From De Filippis et al. (2004).

[v] From Couch et al. (2001).

2.5 m telescope at Las Campanas Observatory. We used the thinned, 2048×2048 Tektronix Tek5 CCD with a 3 e^- count^{-1} gain and 7 e^- read noise. The pixel scale is $0\farcs259$ pixel^{-1} (15 μm pixels), so that the full field of view is $8\farcm8$ on a side, corresponding to 1.8 h_{70}^{-1} Mpc per frame. Data were taken in two filters, Gunn-r ($\lambda_0 = 6550$ Å) and V ($\lambda_0 = 5400$ Å). These filters were selected to provide some color constraint on the stellar populations in the ICL while avoiding flat-fielding difficulties at longer wavelengths and prohibitive sky brightness at shorter wavelengths.

Observing runs occurred on 1998 August 19–25, 1999 September 2–10, and 2000 September 22–27. Specifically, A3888 was observed on the nights of 1999 September 2 and 8 and 2000 September 22–25. Both observing runs took place in the days leading up to new Moon. The night of 1999 September 2 was the only nonphotometric night, and only three cluster images were taken on that night. These were individually tied to the photometric data. The average seeing during the 1999 and 2000 runs was $1\farcs77$ and $0\farcs93$, respectively. Across both runs we observed A3888 for an average of 5 hr in each band. In addition to the cluster frames, night-sky flats were obtained in nearby, off-cluster, "blank" regions of the sky with total exposure times roughly equal to one-third of the integration times on cluster targets. Night-sky flats were taken in all Moon conditions. Typical V- and r-band sky levels during the run were 21.3 and 21.1 mag arcsec^{-2}, respectively.

Cluster images were dithered by one-third of the field of view between exposures. The large overlap from the dithering pattern gives us ample area for linking background values from the neighboring cluster images. Observing the cluster in multiple positions on the chip is beneficial because on combination large-scale flat-fielding fluctuations are reduced. Integration times were typically 900 s as a compromise between signal-to-noise ratio (S/N) and moderating the number of saturated stars.

Observations of the low-redshift clusters will be discussed in a future paper.

4. REDUCTION

In order to create a single, mosaicked image of the cluster with a uniform background level and accurate resolved-source fluxes, the images must be bias and dark subtracted, flat-fielded, flux calibrated, background subtracted, extinction corrected, and registered before combining. These issues are dealt with as described below.

4.1. *Bias and Dark Subtraction*

Preprocessing of the data, including overscan, bias, and dark subtraction, was done in the standard manner using mainly IRAF tasks. The average bias level was stable at $\sim$800 counts, changing by 1% throughout the night. There is structure in the bias in the form of random fluctuations, as well as a highly repeatable, large-scale ramping in the first 500 pixels of every row. To remove this structure, we first fit an eighth-order polynomial to 140 overscan columns and subtract that fit, column by column, from each image. We further average together 10 bias frames per night with 3 σ cosmic-ray (CR) rejection and then boxcar smooth in the vertical direction before subtracting from the data. We choose to smooth in the vertical direction because we have already removed vertical structure in the previous processing step. Test reduction of the bias frames themselves with this procedure reveals no remaining visible structure, and each frame has a mean level of 0 counts to within ± 0.05 counts.

Twenty-five dark exposures were taken per observing run. We averaged these together with a 3 σ rejection to look for structure or significant count levels in the dark current. The mean dark count is 0.6 counts per 900 s, which is less than 0.08% of the sky level and is therefore not significant. However, even at this small count level there is some vertical structure in the dark that amounts to 1 count per 900 s over the whole image. To remove this large-scale structure from the data images, the combined dark frame was median-smoothed over 9×9 pixels ($2\farcs3$), scaled by the exposure time, and subtracted from the program frames. Small-scale variations were not present in the dark. Errors in both the bias and dark subtraction due to structure in the residuals are an additive offset to the background level. These are included in our final error budget based on an empirical measurement of the stability of the background level in the final combined image (see § 7).

4.2. *Flat-Fielding*

The accuracy of any low surface brightness (LSB) measurement is limited by fluctuations on the background level. A major contributor to those fluctuations is the large-scale flat-fielding accuracy. Pixel-to-pixel sensitivity variations were corrected in all cluster and night-sky flat images using nightly, high-S/N, median-combined dome flats with 70,000–90,000 total counts. After this step, a large-scale illumination pattern of order 1% remained across the chip. This was removed using combined night-sky flats of "blank" regions of the sky. To make these night-sky flats, objects in the individual blank-sky frames were first masked before combination. We used SExtractor (Bertin & Arnouts 1996) to identify all sources with a minimum of 6 pixels and a total flux of 2 σ above the sky background. Mask sizes were increased by 4–7 pixels over the semimajor and semiminor axes from the object catalogs to insure object rejection. The masked images were then median-combined with 2 σ rejection. This produced an image with no evident residual flux from sources and kept the large-scale illumination pattern intact. Fluctuations are less than 0.1% peak to peak on $10''$ scales. The final combined night-sky flats were then median-smoothed over 7×7 pixels ($2''$), normalized, and divided into the program images. The illumination pattern was stable among images taken during the same Moon phase. Program images were corrected only with night-sky flats taken in conditions of similar Moon. The contribution of flat-fielding to our final error budget is measured empirically, as described in § 7.

4.3. *Nonlinearity*

Although the ICL measurement is based on a low number of counts, photometric calibration is based on bright standard stars. Accurate calibration is then dependent on the CCD having a linear response to flux. To ascertain whether Tek5 was linear with flux over a wide dynamic range, a consecutive chain of dome-flat images were taken with exposure times of 2–100 s, corresponding to approximately 300–15,000 counts pixel^{-1}. Multiple passes through the exposure time sequence (increasing and decreasing) were made to rule out any effects from fluctuating lamp flux. We find that the Tek5 CCD does have an approximately 2% nonlinearity, which we fitted with a second-order polynomial and corrected for in all the data. The same functional fit was found for both the 1999 and the 2000 data. Note that the exposure times used for all observations are long enough that shutter performance is not a problem. The uncertainty in the linearity correction is incorporated in the total photometric uncertainty discussed below.

4.4. *Photometric Calibration*

Photometric calibration was performed in the usual manner. Fifty to seventy standard stars (Landolt 1992; Jorgensen 1994)

were observed per night per filter over a range of air masses. Stellar magnitudes were measured with an aperture size of 5 times the FWHM, where the FWHM of the stars in the images was determined using SExtractor. We choose this aperture size as a compromise between aperture correction and added background noise. Photometric nights were analyzed together; solutions were found in each filter for a zero point and extinction coefficient with an rms of 0.03 mag (r) in 1999 September and 0.02 mag (r and V) in 2000 September. These uncertainties are a small contribution to our final error budget but are included for completeness as discussed in § 7. Observing the same cluster field for long periods throughout the night allows us to measure an extinction coefficient from stars in the cluster fields, which we find is fully consistent with the extinction coefficient measured from the standard stars. The three exposures taken in nonphotometric conditions were individually tied to the photometric data using roughly 10 stars well distributed around each frame to find the effective extinction for that frame. We find a standard deviation of 0.03 within each frame, with no spatial gradient in the residuals.

We have compared our V- and r-band magnitudes for hundreds of galaxies in the cluster with R-band magnitudes from the Las Campanas AAT Rich Cluster Survey (LARCS; Pimbblet et al. 2002). To the detection limit of the LARCS photometry, and adopting a single average galaxy color to convert between filters, the two samples are consistent with an rms scatter of 0.07 mag.

4.5. *Sky Background Subtraction*

An important issue for accurate surface brightness measurement is the accurate identification of the background sky level. The off-cluster background level in any image is a combination of atmospheric emission (airglow) and light from extraterrestrial sources (zodiacal light, moonlight, starlight, and starlight scattered off of Galactic dust). Zodiacal light comes from solar photons scattered off of ecliptic dust and is therefore concentrated in the ecliptic plane, which, along with the Galactic plane, we were careful to avoid in sample selection, so the extraterrestrial background light will not vary spatially. Light from the extraterrestrial sources will also be scattered into the field of view by the atmosphere. Airglow is emission from the recombination of electrons in the Earth's atmosphere that were excited during the day by solar photons, and as such is a function of solar activity, time elapsed since sunset, and geomagnetic latitude (Leinert et al. 1998). Airglow and atmospheric scattering vary throughout the night, moonlight varies from night to night, and zodiacal light varies from year to year. The background values from frame to frame correspondingly vary temporally by up to 10% throughout one run and 20% from year to year.

Due to the temporal variations in the background, it is necessary to link the off-cluster backgrounds from adjacent frames to create one single background of zero counts for the entire cluster mosaic before averaging together frames. To determine the background on each individual frame we measure average counts in approximately twenty 20×20 pixel regions across the frame. Regions are chosen individually by hand to be a representative sample of all areas of the frame that are more distant than 0.8 h_{70}^{-1} Mpc from the center of the cluster. This is well beyond the radius at which ICL components have been identified in other clusters (Feldmeier et al. 2002; Gonzalez et al. 2005) and is also beyond the radius at which we detect any diffuse light in A3888. The average of these background regions for each frame is subtracted from the data, bringing every frame to a zero background. The accuracy of the background subtraction is discussed in § 7.

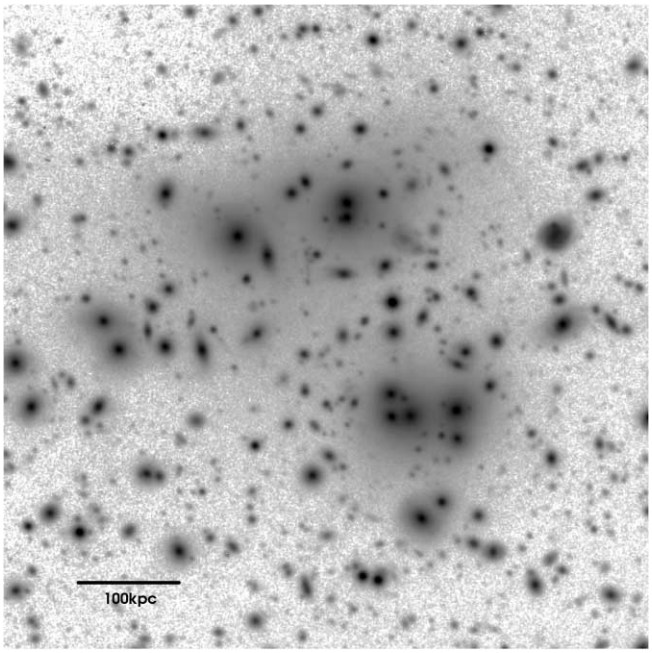

FIG. 1.—Central ~1 Mpc (4.′9) of A3888 in the V band. The gray scale is linear over the range 20.4–29.5 mag arcsec^{-2}. Note the three main groups of galaxies near the center of the cluster. A dozen objects in this image are stars; the rest are galaxies.

4.6. *Extinction Correction*

After background subtraction, all flux in the frame originates above the atmosphere and is subject to atmospheric extinction (large angle scattering out of the line of sight). This is equally true of resolved sources and diffuse sources less than several degrees in extent. While extinction corrections are usually applied to individual resolved sources, that is not possible with the diffuse ICL. We correct entire cluster images for this extinction by multiplying each individual image by $10^{\tau\chi/2.5}$, where χ is the air mass and τ is the fitted extinction term from the photometric solution. This multiplicative correction is between 1.06 and 1.29 for the air-mass range of our A3888 observations.

4.7. *Registration and Distortion*

To combine images we align all 41 individual frames to one central reference frame. SExtractor positions of approximately 10 stars in each frame are used as input coordinates to the IRAF tasks `geomap` and `geotran`, which find and apply x- and y-shifts and rotations between images. The `geotran` solution is accurate to 0.01 pixels (rms). As an independent check of registration accuracy, we confirm that the center coordinates of stars in the original images, as compared to the combined image, are the same to within 0.01 pixels. This uncertainty is negligible for our measurement, which is made on much larger scales. In addition, the ellipticities of individual stars do not change with image combination, suggesting that no systematic errors in registration exist. Stellar ellipticities also show no variation across the frame, suggesting that there are no significant image distortions.

4.8. *Image Combination*

After preprocessing, background subtraction, extinction correction, and registration, we combined the images using the IRAF routine `imcombine` with rejections of -3.5 and $+4.5$ σ. This range was chosen as a compromise between rejecting the CRs and allowing for some seeing variations in the peak flux of

stars. In total, 16 and 25 900 s exposures in the V and r bands, respectively, were averaged together. The final combined image is 4096 pixels (3.6 h_{70}^{-1} Mpc) on a side. The central region (approximately 1 h_{70}^{-1} Mpc on a side) of the final combined V-band image is shown in Figure 1.

5. ANALYSIS

5.1. *Object Detection*

We use SExtractor both to find all objects in the combined frames and to determine their shape parameters. The detection threshold in both the V and r images was defined such that objects have a minimum of six contiguous pixels, each of which are greater than 1.5 σ above the background sky level. This corresponds to a minimum surface brightness of 26.0 mag arcsec^{-2} in V and 26.4 mag arcsec^{-2} in r. The faintest object in the catalog has a total magnitude of 27.0 mag in V and 27.4 mag in r; however, we are complete only to 24.8 mag in V and 24.5 mag in r. We choose these parameters as a compromise between detecting faint objects in high-S/N regions and rejecting noise fluctuations in low-S/N regions. Shape parameters are determined in SExtractor using only those pixels above the detection threshold.

5.2. *Object Removal and Masking*

To measure the ICL we remove all detected objects from the frame by either subtraction of an analytical profile or masking. Details of this process are described below.

5.2.1. *Stars*

Scattered light in the telescope and atmosphere produce an extended point-spread function (PSF) for all objects. To correct for this effect, we determine the telescope PSF using the profiles of a collection of stars from supersaturated 4 mag stars to unsaturated 14 mag stars. The radial profiles of these stars were fitted together to form one PSF such that the extremely saturated star was used to create the profile at large radii and the unsaturated stars were used for the inner portion of the profile. This allows us to create an accurate PSF to a radius of 7′, shown in Figure 2.

The inner region of the PSF is well fitted by a Moffat function. The outer region is well fitted by r^{-3}. There is a small additional halo of light at roughly 50″–100″ (200–400 pixels) around stars imaged on the CCD. Images of saturated stars located off the field of view of the detector do not show this halo, indicating that it is due to a reflection of light off of the CCD itself. We find that roughly 1% of the total flux in the star is in this halo. There are 13 saturated stars within 3.8 Mpc of A3888 ranging from 11.6 to 15.2 V magnitudes. The nearest three saturated stars are 0.6, 0.8, and 1.0 h_{70}^{-1} Mpc from the cluster center and have 14.6, 13.4, and 11.6 V magnitudes, respectively. These stars do not directly contribute to the ICL measurement because they are not near enough to the center, do not have very bright magnitudes, and the PSF does not put very much power into the wings. We do a careful job of background subtraction, by tying to off-cluster flux, so that the PSF also does not affect the background measurement.

For each individual, nonsaturated star we subtract a scaled r^{-3} profile from the frame in addition to masking the inner 30″ of the profile (the region that follows a Moffat profile). Since we do not have accurate magnitudes for the saturated stars in our own data, and to be as cautious as possible with the PSF wings, we have assumed the brightest possible magnitudes for these stars given the full USNO catalog errors. We then subtract a stellar profile with that magnitude and produce a large mask to cover the inner regions and any bleeding. We can afford to be liberal with our saturated star masking, since there are very few saturated stars and none of them are near the center of the cluster, where we need the unmasked area to measure any possible ICL.

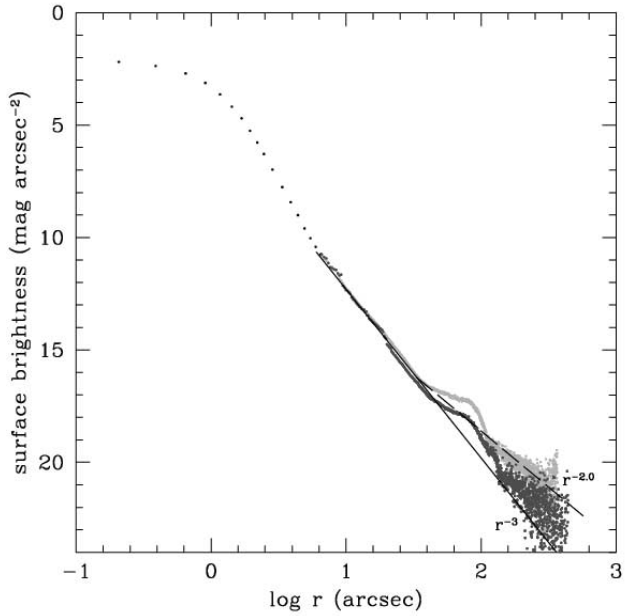

FIG. 2.—PSF of the 100 inch (2.5 m) du Pont telescope at Las Campanas Observatory. The y-axis shows surface brightness scaled to correspond to the total flux of a zero-magnitude star. The profile within 5″ was measured from unsaturated stars and can be affected by seeing. The outer profile was measured from two stars with supersaturated cores imaged in two different positions on the CCD on two different observing runs. The bump in the profile at 100″ is likely related to the position of the star in the focal plane. If the core of a star is imaged off the CCD, its profile does not show this feature, suggesting that the feature is caused by a reflection off the CCD itself. The outer surface brightness profile decreases as roughly r^{-3}, shown by the solid line. An $r^{-2.0}$ profile is plotted to show the range in slopes.

5.2.2. *Galaxies*

To make an ICL measurement we would ideally like to subtract a scaled analytical profile for each galaxy that would leave no residuals and would allow us to recover the area on the sky covered by cluster galaxies. We have attempted to do this using three publicly available algorithms: GIM2D (Simard et al. 2002), GALFIT (Peng et al. 2002), and the IRAF task `ellipse` (Jedrzejewski 1987). With these algorithms, we have employed a wide range of surface brightness profiles, including de Vaucouleurs, Sérsic, exponential profiles, and combinations thereof. In addition, we have used iterative techniques to alternately fit and remove galaxies in crowded fields. The technical challenges in fitting the galaxies, including galaxy deblending, PSF effects and deconvolution, two-dimensional profile fitting, and speed in performing many Fourier transforms, have been previously discussed by several groups (see, e.g., Peng et al. 2002 for a review).

Figure 3 shows representative results of modeling three galaxies using GALFIT: one isolated galaxy and two galaxies in increasingly dense regions. These examples show that the algorithms perform well for isolated galaxies but fail for galaxies near the core either because of the difficulty in deblending many overlapping galaxy profiles or because the individual galaxies in such dense regions do not follow simple analytical profiles. It is not clear what the profiles should be of galaxies deep in the

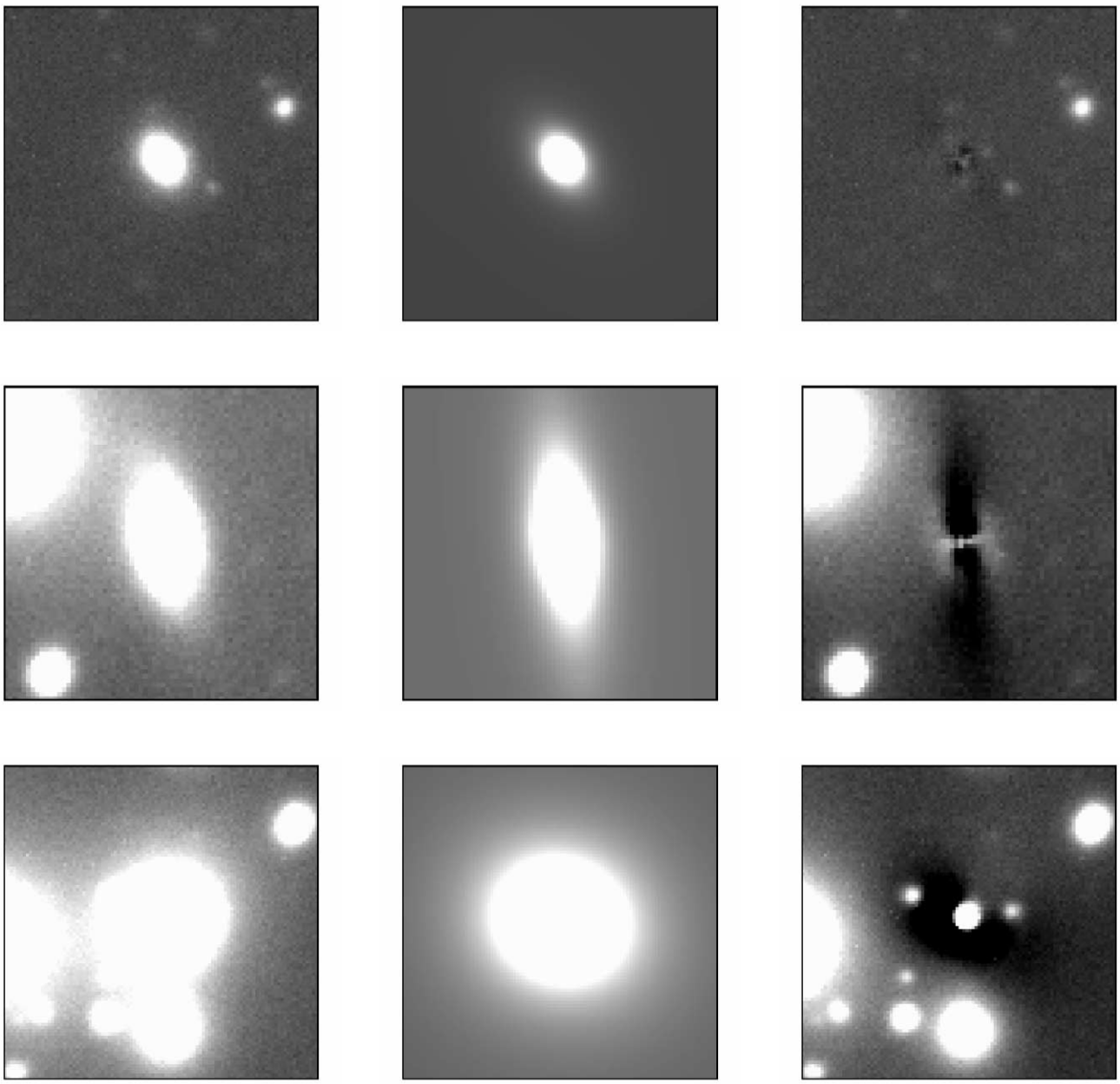

FIG. 3.—Images of observed galaxies, GALFIT models, and model-subtracted residual images shown from left to right for three different galaxies in A3888. All images are shown at the same surface brightness levels. The top row shows a fairly isolated galaxy in the outer regions of the cluster, which is well modeled by GALFIT. The middle and bottom rows show galaxies in increasingly denser environments, depicting well the limitations of galaxy modeling algorithms for galaxies in very dense regions.

potential wells of clusters (Trujillo et al. 2001; Feldmeier et al. 2004). The fact that A3888 is not a relaxed cluster clearly makes galaxy subtraction more difficult near the core than it would be in a cD cluster; A3888 has three main brightness peaks, which contain 3, 7, and 12 galaxy cores in their densest regions, respectively.

As it is not possible to cleanly fit the galaxies in this cluster such that the residuals (positive or negative) do not interfere with the ICL measurement, we have chosen to mask the galaxies. This gives us a well-defined measurement of the ICL at the expense of forfeiting some area. Although we could model and subtract the more isolated galaxies in the outer regions of the cluster, it is in these regions that we can generously mask the galaxies and still have enough pixels for an ICL measurement. Note that we do not replace masked pixels. Masked regions are simply removed entirely from the ICL measurement.

We use the same masks for both bands so that all galaxies are masked to the same radius, thereby ensuring a self-consistent measurement of the ICL color. We use the *r*-band image to define the masks, as it has a deeper detection threshold (and thus larger detection areas) than the *V*-band catalog. Objects are identified using SExtractor, and masks are based on the isophotal detection area with a threshold of 26.4 mag arcsec^{-2} (1.5 σ above sky). To be conservative in rejection, we scale the semimajor and semiminor axes identified by SExtractor to increase the area of each galaxy mask by a multiplicative factor of 2–2.3, depending on the magnitude of the galaxy. To explore the effect of mask size on the profile shape of the ICL, we make two additional images with mask sizes that are 30% smaller and 30% larger than the original masks. We then measure the ICL three times with the three versions of mask sizes. Additional minor masking is done by hand to remove any remaining flux associated

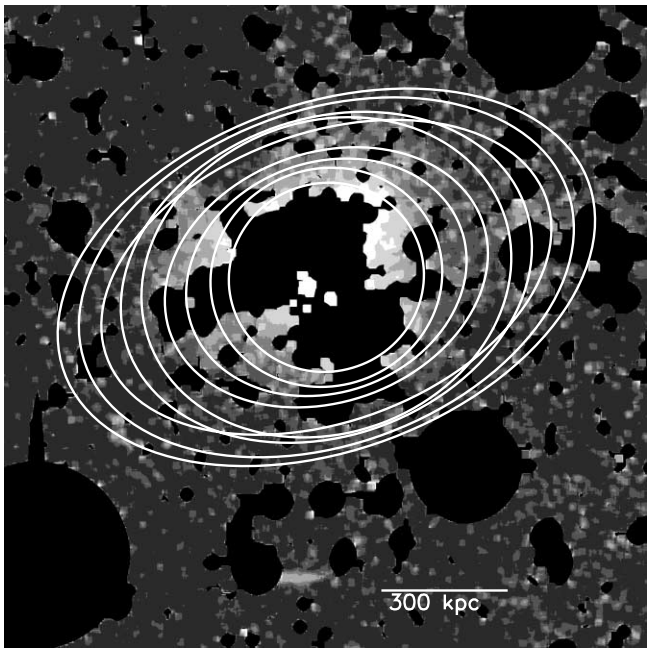

FIG. 4.—Fully masked, final *V*-band image of the central 1.5 h_{70}^{-1} Mpc (7′.3) of A3888, smoothed to aid in the visual identification of surface brightness levels. Masks are shown in their intermediate size; see § 5.2.2. Large circular masks correspond to the locations of bright stars. The six gray-scale levels show surface brightness levels of up to 28.5, 27.7, 27.2, 26.7, and brighter than 26.2 mag arcsec^{-2}. The `ellipse` isophotes are overlaid from 65″ to 190″. The tidal feature, C, also shown in Fig. 11, is clearly visible at center near the bottom of the image.

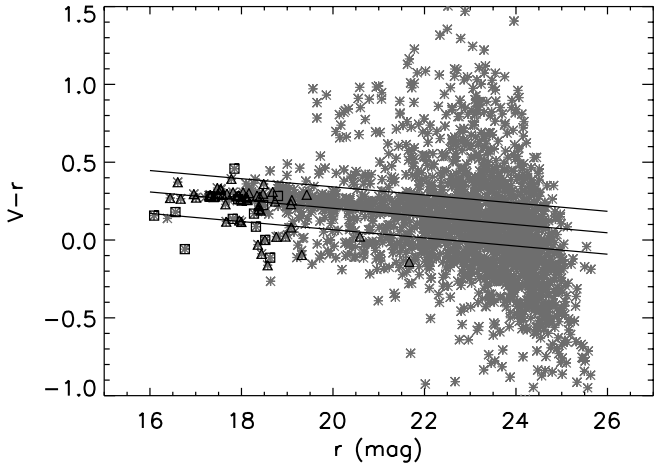

FIG. 5.—Color-magnitude diagram of galaxies in A3888. All galaxies detected in our data are plotted with gray symbols. Those galaxies that have membership information in the literature are overplotted with open triangles (members) or squares (nonmembers). The red sequence is clearly visible. Solid lines indicate a biweight fit to the red sequence with 1 σ uncertainties.

with resolved objects. These few regions are associated with small overlapping sources that are not correctly deblended by SExtractor.

The total masked area within the central 1.2 Mpc of the cluster in each of the three mask sizes is 34%, 41%, and 49%, respectively. The masked fraction is much higher in the very center of the cluster and reaches nearly 100% in the inner 30″. The increase in the masked fraction is not directly proportional to the increase in mask size because the masks often overlap. Figure 4 shows the final *V*-band image with intermediate-sized masks.

5.3. *Cluster Membership and Flux*

An interesting characteristic of the ICL lies in its comparison to cluster properties that include the cluster galaxies themselves. We compare two methods below for measuring cluster membership and flux: (1) we identify member galaxies using our own two-band photometry; and (2) we integrate the flux in a published galaxy luminosity function for this cluster.

Some published velocities are available in the literature (Teague et al. 1990; Pimbblet et al. 2002) and can be used to explicitly identify member galaxies. However, these redshift surveys are not complete to our detection threshold and therefore cannot provide membership information for all detected galaxies. Alternatively, we can estimate cluster membership using a color-magnitude relation (Fig. 5) from our *V* and Gunn-*r* images. There is a clear red sequence of galaxies in which the brightest galaxies have $V - r = 0.3 \pm 0.15$. Those galaxies that lie within 1 σ of a biweight fit to the red sequence are taken to be cluster members (functional form taken from Beers et al. 1990). The slope of the red sequence is 0.1 mag (color)/4 mag (galaxy *r*-magnitude). Those galaxies that are redder than the red sequence are both generally fainter, implying that they are higher redshift background galaxies, and not as concentrated toward the center of the cluster as all galaxies. The number of those very red galaxies per projected area is 38% ± 11% higher within 400 kpc than without. Although some of these galaxies are undoubtedly members of the cluster, their spatial distribution does not allow us to make conclusive statements about their membership. Approximately 42% of the galaxies in the image are identified as members by this method. Of the galaxies with spectroscopically determined velocities, 78% of the 55 confirmed members are included in the cut; 54% of the 13 known nonmembers are also included. The red cluster sequence is a good tool for identifying clusters, but it is not a perfect method of determining membership, as it is unable to cleanly distinguish between member and nonmember galaxies.

We measure the total flux in all galaxies identified as members using corrected isophotal magnitudes from SExtractor. For these, SExtractor assumes a Gaussian profile to infer the flux beyond the isophotal detection threshold, corresponding to 26.0 *V* mag arcsec^{-2} and 26.4 *r* mag arcsec^{-2}. As expected, the corrected magnitudes are brighter than the isophotal magnitudes by a full magnitude at the faint end of our detection limit. The total flux in galaxies within 700 h_{70}^{-1} kpc of the center of the cluster, as determined from the same galaxy catalog that was used for galaxy masking, is $3.9 \times 10^{12}\ L_{\odot}$ in the *V* band and $4.9 \times 10^{12}\ L_{\odot}$ in the *r* band. We expect the error on the total flux from this estimate to be greater than 30%, which is mainly due to uncertainty in the membership determination.

We can also determine cluster flux using the Driver et al. (1998) luminosity distribution for this cluster, which is based on a statistical background subtraction of noncluster galaxies. It would be possible to do this with our own data; however, Driver et al. (1998) have more uniform, large-area coverage to several magnitudes below M_* at the redshift of the cluster. In addition, the authors pay careful attention to observing background fields that are up to 75′ from the cluster center, at approximately the same air mass, seeing, exposure time, and UT as the cluster fields. Consequently, the background fields have the same noise characteristics and detection threshold as the cluster images and sample the same large-scale structures. They can therefore be used to reliably determine the contamination of the cluster fields. Bernstein et al. (1995) give a careful account of the significant

considerations in using this method, all of which are taken into account by Driver et al. (1998).

We explore one minor effect not discussed by Driver et al. (1998): the effect of gravitational lensing on the background galaxy counts. There are two competing effects that change the number and brightness of galaxies behind the cluster as compared to background galaxy counts in an off-cluster field. First, magnification of the background galaxies will artificially inflate the background counts behind the cluster, resulting in an underestimation of cluster galaxy flux. Second, all background objects behind the cluster will appear radially more distant from the cluster center, which will artificially decrease the background counts, resulting in an overestimate of the cluster galaxy flux. The change from an overall magnification to demagnification happens at $z \simeq 0.5$. Following the method of Broadhurst et al. (1995) to determine the strength of the demagnification for A3888 at $z = 0.15$, we find a negligible degradation in the *V*- and *r*-band flux (<0.2%) and therefore do not correct for it in the Driver et al. (1998) background counts.

Driver et al. (1998) use their *R*-band luminosity distribution to determine a dwarf-to-giant ratio; however, we choose to fit it with a classical Schechter function ($M_R^* = -22.82 \pm 0.28$, $\alpha = -0.97 \pm 0.09$, and $\chi_\nu^2 = 0.71$), which can then be used to determine a luminosity density for the cluster. We note that the luminosity distribution is not perfectly fitted by a Schechter function at the bright end, due mainly to a small number of extremely bright galaxies, as is typical of clusters. Adopting a volume equal to that over which we are able to measure the ICL, 1.4 Mpc^3, and integrating the luminosity function down to very faint dwarf galaxies, $M_R = -11$, the total luminosity from galaxies in the cluster is $(5.9 \pm 0.94) \times 10^{12}\ L_\odot$ in the *R* band. Given galaxy colors from Fukugita et al. (1995), the total luminosity from galaxies in A3888 is $(3.4 \pm 0.6) \times 10^{12}\ L_\odot$ in *V* and $(4.3 \pm 0.7) \times 10^{12}\ L_\odot$ in the *r* band. The difference between this value of total flux and that determined from our color-magnitude estimate of membership is likely due to uncertainties in our membership identification and differences in the detection thresholds of the two surveys. Although the two estimates are generally consistent, we adopt the total flux as derived from the luminosity distribution throughout the remainder of the paper.

6. RESULTS

6.1. *Surface Brightness Profile*

After subtracting the stars and masking the galaxies, we fit the resulting image with the IRAF routine `ellipse`, a two-dimensional, interactive, isophote-fitting algorithm. Again, the masked pixels are completely excluded in this procedure. There are three free parameters in the isophote fitting: center, position angle, and ellipticity. We fix the center (R.A. = $22^{\rm h}34^{\rm m}26\overset{\rm s}{.}0$, decl. = $-37^\circ44'07\overset{''}{.}2$ [J2000.0]) and position angle (-70°) to values found by `ellipse` based on the inner isophotes and let the ellipticity vary as a function of radius. Fitted ellipticities range from 0.2 to 0.5. Allowing the center and position angle to vary results in worse fits. Stable fits are found from $60''$ to $250''$. From the fitted isophotes we identify a fairly smooth ICL profile over the range of 26 to approximately 29 mag arcsec^{-2}. The error on the mean within each elliptical isophote is negligible, as discussed in § 7. It is possible that the different seeing in the *V*- and *r*-band images could unevenly affect the profiles. To address this issue, the *V*- and *r*-band images have been convolved to the same seeing and the surface brightness profiles remeasured. No significant change was found in the profiles.

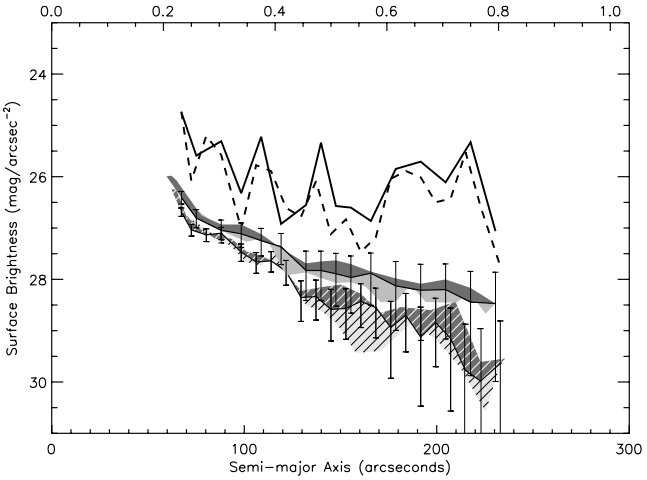

FIG. 6.—Surface brightness profile of the ICL, as well as the total cluster light plotted as a function of distance along the semimajor axis in arcseconds. The axis at the top of the figure indicates the corresponding physical scale in h_{70}^{-1} Mpc. We plot both *V*- and *r*-band data together for comparison. The bottom two lines on the plot are the ICL profiles; the *r*-band light is surrounded by filled shading, and the *V* band is surrounded by hatched shading. The shadings show the difference in ICL profiles produced by increasing or decreasing the area of the galaxy masks, as discussed in § 5.2.2. The top two lines (without shading) represent the total cluster light as measured in the same elliptical isophotes as the ICL; the dashed line represents the *V*-band light, and the solid line represents the *r* band. Also shown are the cumulative 1 σ errors for both bands as discussed in § 7 and summarized in Table 3.

Note that we are not able to measure the ICL at radii smaller than $60''$ because that region is heavily masked. Most other ICL measurements focus on this inner region, leaving little overlap between this survey and previous work in other clusters. In clusters containing a cD galaxy, the diffuse component of the cluster has been found to blend smoothly into the cD envelope, and masking in the core of such clusters is not necessary (see most recently Gonzalez et al. 2005).

We identify the surface brightness profile of the total cluster light (i.e., including resolved galaxies) for comparison with the ICL within the same radial extent. To do this, we make a new "cluster" image, with color-determined, nonmember galaxies masked out (see § 5.3). A surface brightness profile of the cluster light is then measured from this image using the same elliptical isophotes as were used in the ICL profile measurement. This profile, in contrast to the ICL, is quite irregular, reflecting the clustering of galaxies. Substructure in the galaxy distribution is an indication of a young dynamical age for this cluster.

Figure 6 shows the surface brightness profiles of the ICL, as well as the total cluster light as a function of semimajor axis in both the *V* and *r* bands. Results based on all three versions of mask size (as discussed in § 5.2.2) are shown. The uncertainty in the ICL surface brightness is dominated by the accuracy with which the background level can be identified, as discussed in § 7. Error bars in Figure 6 show the cumulative uncertainties in Table 3.

Two characteristics are evident from the surface brightness profiles. First, the inner region (200–400 h_{70}^{-1} kpc) has a notably steeper profile than the outer region. While the entire profile can be adequately described within the 1 σ uncertainties by a single exponential, a double exponential gives a better fit in the *r* band (χ_ν^2 improves by 50%) and a marginally better fit in the *V* band. These fits are shown in Figures 7 and 8. We have also fitted the ICL profile with de Vaucouleurs and Sérsic profiles. Acceptable

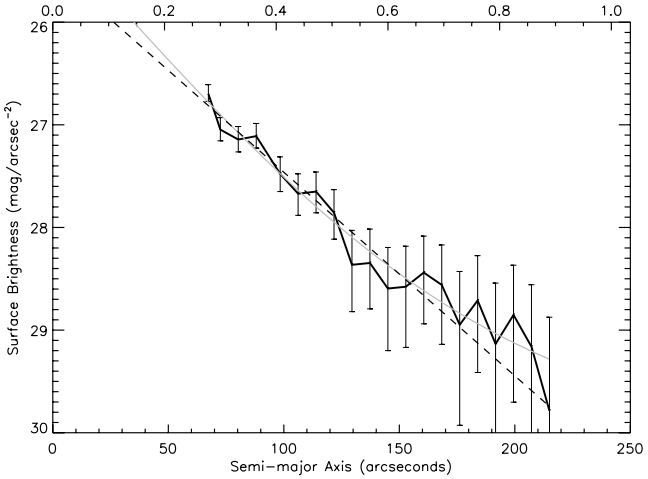

FIG. 7.—*V*-band ICL and 2 σ error bars overplotted with exponential fits. The best-fit single (*dashed line*) and double (*gray line*) exponentials are shown.

fits can be found; however, the best-fit values are unphysical, namely, they have high exponents for the Sérsic and unrealistically large effective radii for the de Vaucouleurs profiles. The second general characteristic of the ICL is that it is more concentrated than the galaxies, which is to say that the ICL falls off more rapidly with radius than the galaxy light.

6.2. *Spatial Distribution*

The ICL is aligned to within 10° of the position angle of the hot intracluster gas. Figure 9 shows contours of *XMM-Newton* archival observations overlaid on our optical image. We interpret the alignment of the diffuse ICL with the hot gas in the cluster as an indication that we are indeed measuring light that follows the gravitational potential of the cluster. In addition, the ICL radial surface brightness profile is significantly different from the galaxy surface brightness profile in both *V* and *r*, suggesting that the ICL component is at least in part distinct from the individual galaxies in the cluster.

6.3. *Color*

We measure an average $V - r$ color of the ICL by binning together three to four points from the ICL radial profile. Between 200 and 400 h_{70}^{-1} kpc, the innermost measured radii, the diffuse ICL has an average color of $V - r \simeq 0.3 \pm 0.1$. Beyond 400 h_{70}^{-1} kpc the ICL becomes increasingly redder such that by 700 h_{70}^{-1} kpc the ICL has an average color of $V - r \simeq 0.7 \pm 0.4$. The only characteristic color of the galaxies we have to compare with the ICL is the red-sequence color ($V - r = 0.3 \pm 0.15$). We have no definitive membership information for those galaxies off the red sequence. The color of the ICL in the inner 400 h_{70}^{-1} kpc is roughly equivalent to the red elliptical galaxies residing in the same part of the cluster but significantly redder than several tidal features we detect (see § 6.5). The color of the ICL beyond 400 h_{70}^{-1} kpc is redder than the red-sequence galaxies. The color of the diffuse ICL can be approximated as a simple linear function of radius, with a slope of +0.1 per 100 h_{70}^{-1} kpc and a *y*-intercept of −0.1. Figure 10 shows the color profile and corresponding 1 σ error bars. While this fit is clearly simplistic,

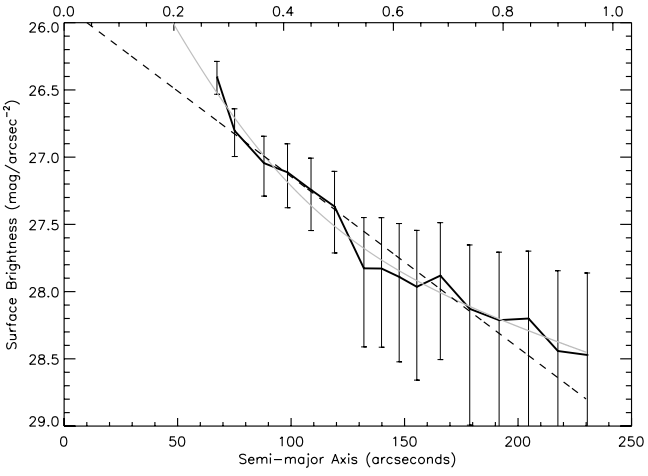

FIG. 8.—Same as Fig. 7, but in the *r* band.

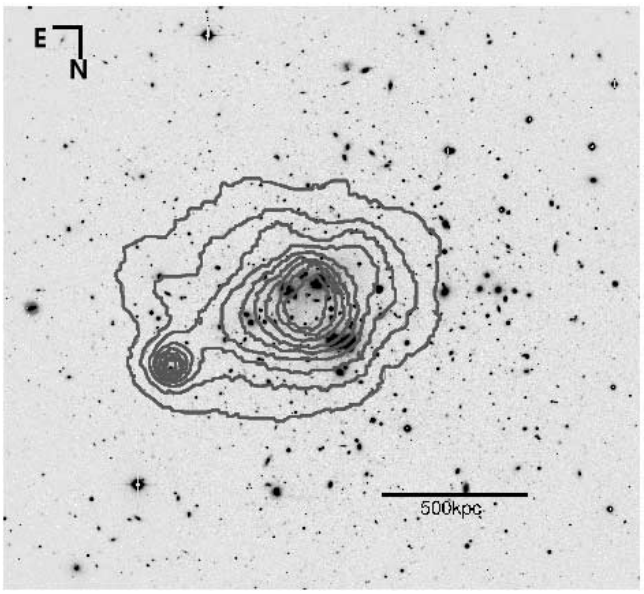

FIG. 9.—X-ray contours taken from *XMM-Newton* archival data overlaid on our *V*-band optical image. Logarithmic contours are shown from 1 to 20 counts. The bright point source 600 h_{70}^{-1} kpc from the cluster center is a Seyfert I galaxy.

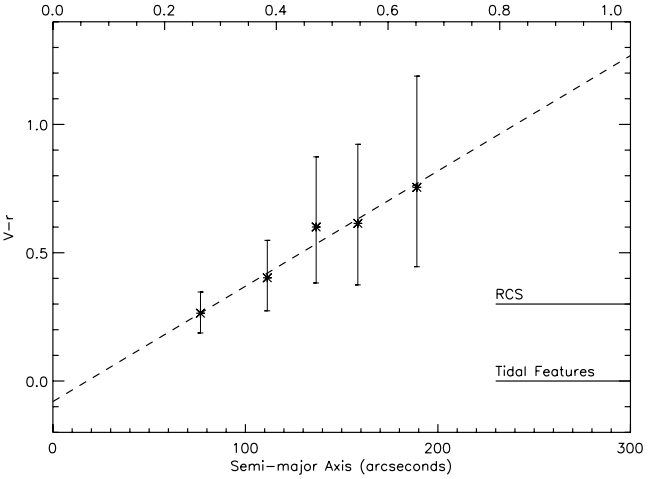

FIG. 10.—ICL color vs. radius in coarse radial bins based on the surface brightness in *V* and *r*, as shown in Fig. 6. The lower axis shows the radius in arcseconds, and the upper axis shows the radius in megaparsecs. The dashed line is the best-fit linear function. The average colors of the red cluster sequence and the tidal features are also shown for comparison.

the data do not warrant a more complicated fit. This red color gradient is the opposite of what we expect to find for the cluster galaxies. When looking at the color of galaxies as a function of distance from the center of the cluster, we find a flat or slightly blueward profile such that the galaxies get slightly bluer with increasing radius. Therefore, the ICL color profile is distinct from the galaxy color profile.

Using the population synthesis models of Bruzual & Charlot (2003) we can obtain rough constraints on the age and metallicity of the stellar population that contributes to the ICL. Because the total range in color is not large and because the age-metallicity degeneracy limits our conclusions, we limit our discussion to two regions, $r < 400\ h_{70}^{-1}$ kpc and $r > 400\ h_{70}^{-1}$ kpc, rather than individual points along the full radial profile. The stellar evolution models begin with a starburst of user-defined strength and extent, a Salpeter initial mass function, and a standard ΛCDM universe. The stars then evolve along the Girardi et al. (1996) spectral evolution tracks. Within this scheme, the simplest scenario is an instantaneous starburst with a single formation epoch and metallicity. For this case, the red color of the ICL in the outer 400–700 h_{70}^{-1} kpc, $V - r \sim 0.6$, is consistent with a stellar population that formed at redshifts $1 < z_f < 10$ (7–13 Gyr ago) with an initial abundance of $1.0\ Z_\odot < Z_{\rm ICL} \lesssim 2.5\ Z_\odot$. The color of the ICL in the inner 200–400 h_{70}^{-1} kpc, $V - r \sim 0.3$, allows the minimum age of that range to be lowered, where the most recent allowable formation is ∼5 Gyr ago ($z_f < 1$) with an initial abundance of 0.2–0.5 times the solar value. Allowing an extended burst of 10–100 Myr duration has a minimal effect on the $V - r$ color. Allowing an exponentially decaying starburst with an *e*-folding time of 1 Gyr, the population becomes 0.02–0.06 mag bluer overall, depending on the initial formation redshift. For the ICL in A3888, an exponential star formation history therefore implies even higher metallicities or earlier formation. Finally, simulations with a constant star formation rate of $1\ M_\odot\ {\rm yr}^{-1}$ create very blue stars. It is not possible to form a stellar population with a constant star formation rate that has $V - r = 0.6$. Implications of these models are discussed further in § 8.1.

6.4. *Fractional Flux*

The ratio of ICL flux to total cluster flux can help constrain the importance of galaxy disruption in the evolution of clusters. To identify the total flux in the ICL, we integrate the single exponential fit to the ICL surface brightness profile (see § 6.1) over the range 0″–200″(∼700 h_{70}^{-1} kpc). As we are not able to measure the ICL at radii smaller than ∼60″, this requires an extrapolation into the center of the cluster. Note that the single exponential fit, which is dominated by the slope of the ICL profile at larger radii, gives significantly less light in the core than the double exponential fit (see Figs. 7 and 8) and is therefore a conservative estimate of ICL flux. The total flux in the ICL is then $(4.5 \pm 1.3) \times 10^{11}\ L_\odot$ in *V* and $(5.9 \pm 2.2) \times 10^{11}\ L_\odot$ in *r*, where the errors are the full errors as described in § 7. This value is equivalent to the full disruption of roughly $7L_*$ galaxies.

We consider four modifications to this estimate of the total ICL flux. First, we consider a correction for that volume of the cluster filled with galaxies, since no ICL can exist in that volume. While lines of sight intersect galaxies over most of the area near the center of the cluster, the galaxy filling factor is less than 3% by volume, even inside 200 h_{70}^{-1} kpc (60″, projected). So it is reasonable to assume that intracluster stars do exist in that volume and we need make no correction for the filled volume. Second, we can determine a hard lower limit to the ICL flux by assuming that there is *no* ICL in the inner 60″. This correction, albeit extreme, would decrease our estimate of the total ICL flux by 30%. Third, we make a less extreme correction by assuming a flat core region instead of the exponential extrapolation. A flat profile is suggested by Aguerri et al. (2005), although those results are in Virgo, where the center of the ICL is not defined and the measurement is based on small area coverage, which does not allow for an elliptical profile determination. A flat core region would decrease our estimate of the total ICL flux by 5%. Fourth, we consider LSB galaxies below our detection threshold that could contribute to, and therefore be an error in, the inferred ICL flux. To account for these very faint galaxies, we integrate the cluster galaxy luminosity function from our detection limit ($M_R = -15.22$) to $M_R = -11.0$. Due to the extremely low detection threshold of this survey (7.6 mag below M_*) and the apparently flat faint end of the luminosity function ($\alpha = -0.97$; see § 5.3), only 0.07% of the total galaxy flux could come from galaxies this faint. As this contribution is not significant, we make no correction for this effect.

Adopting the total galaxy flux found from the luminosity function in § 5.3, we find that the ICL accounts for 13% ± 4% of the total *V*-band cluster light and 13% ± 5% of the *r*-band cluster light within 700 h_{70}^{-1} kpc of the center of the cluster. The range in these values comes from the combination of all uncertainties in the ICL measurement coupled with the uncertainty in the total cluster flux, as discussed in § 7. The galaxy light and the ICL decrease with radius, but since we do not accurately know the slope of either of them at large radii, we compare fluxes within the same volume over which we have reliable data. This fraction is only relevant at this radius and is likely to be lower when taking into account the entire virial radius of the cluster, since the ICL is centrally concentrated and not evenly distributed throughout the cluster. On the same note, ICL measurements at smaller radii are likely to find a higher fraction of the total flux in the ICL because of the steep ICL profile and because the volume involved is much smaller. For example, if we assume that we can only measure the ICL in the inner 600 h_{70}^{-1} kpc instead of 700 h_{70}^{-1} kpc, we find a fractional flux of 19% in both *V* and *r*, an almost 50% increase over the measured 13%.

6.5. *ICL Substructure*

Using the technique of unsharp masking, we find three possible tidal features, all within the central 500 h_{70}^{-1} kpc of A3888, identified as A, B, and C in Figure 11. Arcs A and B are both roughly 15 h_{70}^{-1} kpc × 5 h_{70}^{-1} kpc and are near to the center of the cluster. Arc C is a diffuse, tail-like feature at 500 h_{70}^{-1} kpc from the center and covers 130 h_{70}^{-1} kpc × 20 h_{70}^{-1} kpc (see Table 2). All three features are blue, $V - r \simeq 0.0$, with a combined flux equivalent to one $r = 20.8$ mag galaxy ($0.1M_*$). These objects are unlikely to be gravitational arcs, since they are not oriented tangentially to the cluster potential.

The diffuse nature of the large feature, C, suggests that it is tidal. This object is very similar to the large arcs found in Coma, Centaurus, and A1914 (Gregg & West 1998; Calcáneo-Roldán et al. 2000; Feldmeier et al. 2004), which are included in Table 2 for reference. In general, it is of similar size to, but slightly fainter than, those found in the other clusters. It has slight curvature and appears to connect to a pair of galaxies (Fig. 11, *bottom*, *left side*) that could be in the midst of an interaction. Both Calcáneo-Roldán et al. (2000) and Feldmeier et al. (2004) find through numerical simulations that these types of arcs are typical of recent tidal interactions between luminous spiral galaxies and massive cluster elliptical galaxies. Spectroscopy to confirm its origin at this faint surface brightness is not currently possible.

We cannot rule out the possibility that the two smaller features in our 0.06 $\deg^2$ of cluster imaging are LSB galaxies seen

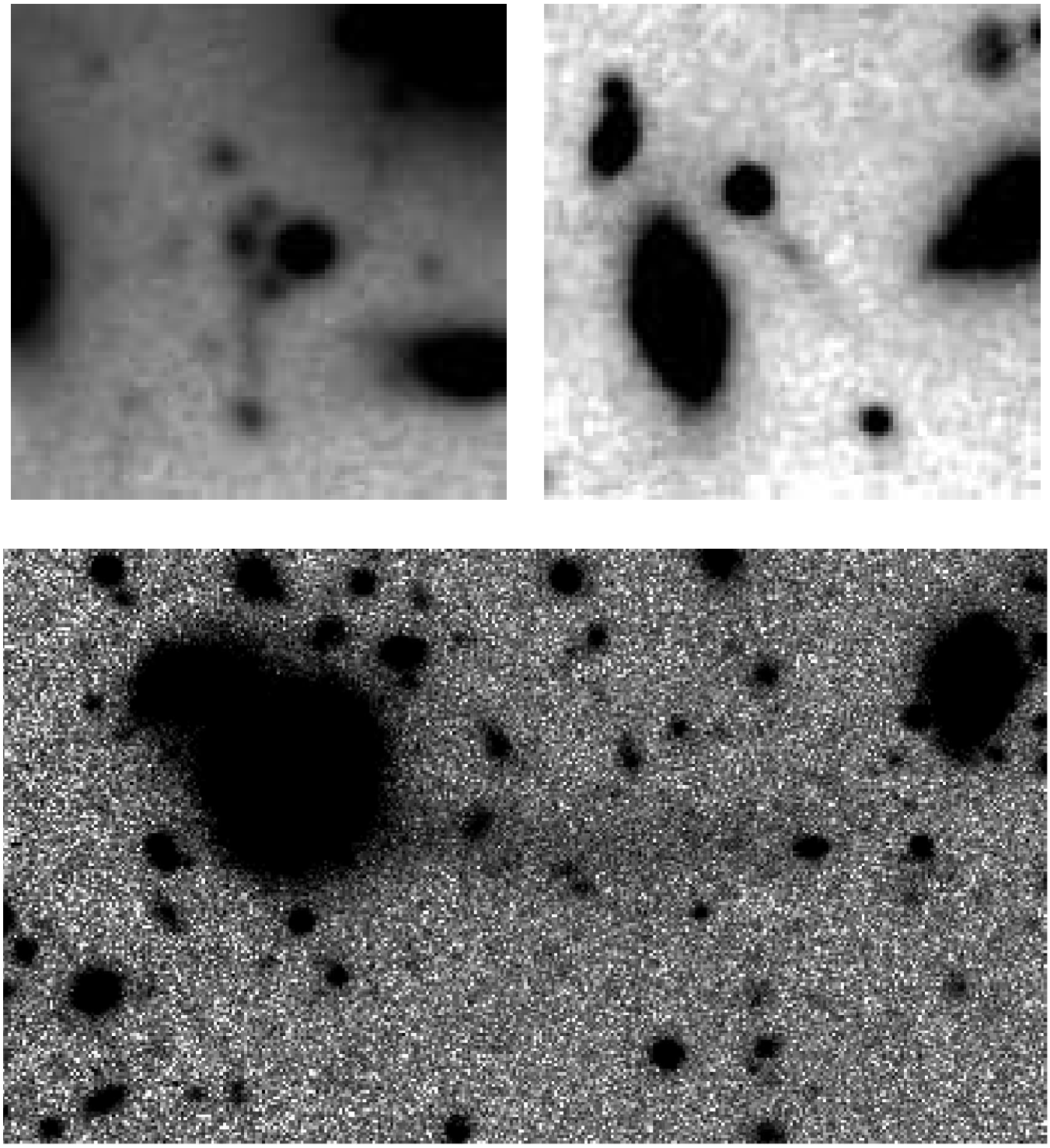

FIG. 11.—Three LSB features from the final *V*-band image. The top two panels show features located near the center (features A and B in Table 2). The bottom image shows the larger feature (C) located 500 h_{70}^{-1} kpc from the center of the cluster.

edge-on. In field surveys, surface densities of the dimmest LSB galaxies (23 V mag arcsec^{-2} $< \mu_0 <$ 25 V mag arcsec^{-2}) are at least 0.01 galaxies deg^{-2} (Dalcanton et al. 1997). In clusters, although there are overall higher space densities of galaxies, LSB galaxies run the risk of getting tidally disrupted in the harsh environment of cluster centers. In a survey of the Cancer and Pegasus clusters, O'Neil et al. (1997) find 1.6 galaxies deg^{-2} with central surface brightnesses dimmer than 21.2 in V. The two candidates with average surface brightnesses of roughly 25 mag arcsec^{-2} in V in this cluster represent a higher density than is found in these surveys. In addition, they do not have clear centers. Both of these facts suggest that they are not LSB galaxies. However, it is likely that even if these are LSB galaxies, they will not remain bound systems for long in the high-density cluster environment, and we therefore consider them to be contributors to the ICL in the following calculation.

We briefly examine the importance of all three tidal features in contributing to the ICL over a Hubble time to see whether

TABLE 2
SUBSTRUCTURE IN A3888

Object	Radial distance (h_{70}^{-1} kpc)	Length (h_{70}^{-1} kpc)	Width (h_{70}^{-1} kpc)	$V-r$	M_V	M_r	$\mu(V)$ (mag arcsec^{-2})	$\mu(r)$ (mag arcsec^{-2})
A	66	17	5	−0.05	−18.5	−18.5	24.6	24.5
B	155	15	5	0	−18.1	−18.1	25.3	24.9
C	720	132	20	0.03	−20.5	−20.5	26.4	26.7
Coma[a]	100	130	15–30	0.57(R)	−18.8	−19.4(R)	26.9	26.3(R)
Centaurus[b]	170	171	1	...	...	−14.8(R)	...	26.1(R)
A1914[c]	75	160	30	...	...	...	26.1	...

[a] From Gregg & West (1998).
[b] From Calcáneo-Roldán et al. (2000).
[c] From Feldmeier et al. (2004).

they can account, in whole or in part, for the ICL found in the cluster. Cluster-crossing time is estimated to be 4.5 Gyr given a virial radius of 3.7 Mpc and a temperature of 10 keV (Reiprich & Böhringer 2002). We assume both a constant rate of formation and the dissipation of tidal features in approximately one crossing time. From this we conclude that in one Hubble time approximately one-half of an M_* galaxy will be contributed to the ICL through visible tidal features such as these. This simple calculation suggests that these features cannot account for the current ICL flux; however, it is feasible that there was a variable interaction rate in the history of this cluster. Further substructure could also be hidden below our surface brightness detection threshold.

At the distance of A3888, the flux of a single globular cluster ($M_V \gtrsim 10$ mag) spread over one seeing disk (3.5 h_{70}^{-1} kpc) is many magnitudes below our surface brightness detection threshold. Therefore, we are not sensitive to intracluster globular clusters that have been studied by other groups in nearby clusters (Jordán et al. 2003; Bassino et al. 2003; Hilker 2003; Marín-Franch & Aparicio 2003).

6.6. *Group*

In addition to the main cluster ICL, we detect excess diffuse light around a group of galaxies that are 1.35 h_{70}^{-1} Mpc from the center of A3888, R.A. = $22^{\rm h}34^{\rm m}48\overset{\rm s}{.}5$, decl. = $-37^\circ39'19\overset{''}{.}58$ (J2000.0). There are two galaxies centered in this diffuse component, separated by only 2″. The spatial extent of the group appears to be 200 h_{70}^{-1} kpc, within which there are 60 galaxy peaks detected by SExtractor. Independent of the ICL component, the group is identified in the density distribution of the cluster. Velocities are available only for the central galaxies in the group; however, these suggest that the group is cospatial with A3888 (Pimbblet et al. 2002; Teague et al. 1990). Within the 200 h_{70}^{-1} kpc extent of the group, we find $1.7\times10^{10}\ L_\odot$ in V and $2.6\times10^{10}\ L_\odot$ in r above background, which is equivalent to approximately 20% of an M_* galaxy.

The average color of this diffuse component based on total flux within 200 h_{70}^{-1} kpc is $V-r=0.5$, which is again redder than the cluster galaxies and consistent with the color of the main cluster ICL at large radii. The accuracy of the fluxes and hence the colors is limited by the accuracy in masking, since it is a simple sum over the pixels in the group region. We estimate the error in masking to be less than 30% based on our work with varying the mask size (see § 6.1 and Table 3).

This secondary ICL concentration is consistent with galaxy interactions and ram pressure stripping occurring in an infalling group (“preprocessing”). Such preprocessing has been shown in simulations to affect galaxies before they fall into the main cluster potential (Willman et al. 2004; Fujita 2004, and references therein). This is also consistent with recent measurements of a small amount of ICL in isolated galaxy groups (Castro-Rodríguez et al. 2003; Durrell et al. 2004).

7. ACCURACY LIMITS

The accuracy of the ICL surface brightness is limited on small scales (<10″) by photon noise. On larger scales (>10″), structure in the background level (be it physical on the sky or instrumental) will dominate the error budget. We determine the stability of the background level in the image on large scales by first median-smoothing the masked image by 75″. We then measure the mean flux in thousands of random 1″ regions more distant than 0.8 Mpc from the center of the cluster. The standard deviation of these regions is 29.5 mag arcsec^{-2} in V (0.06% of sky) and 28.8 mag arcsec^{-2} in r (0.01% of sky). Histograms with Gaussians overlaid are shown in Figures 12 and 13. The histograms are not perfect Gaussians. This is likely due to the fact that the background level includes both a symmetric Gaussian and positive sources that are below the detection threshold. The offset of the Gaussian portion of the histogram represents the statistical difficulty in measuring the mean value of the background in any one image. Regions from all around the frame are used to check that our accuracy limit is universal across the image and not affected by location in the frame. This empirical measurement of the large-scale fluctuations across the image is dominated by the instrumental flat-fielding accuracy but includes

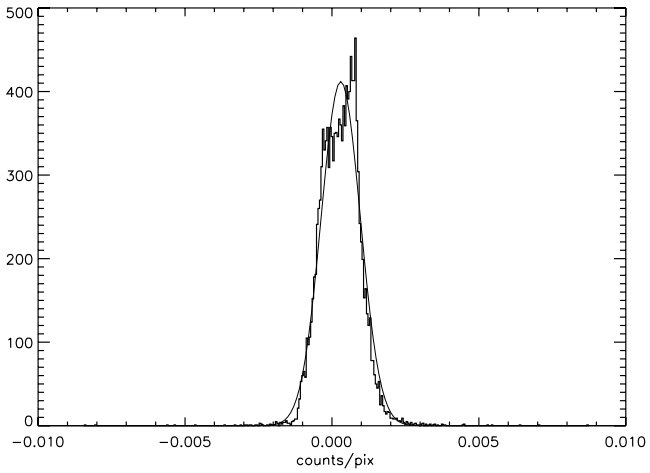

FIG. 12.—Histogram of the mean count values in 1″ × 1″ regions in the fully masked V-band image. All regions are greater than 800 h_{70}^{-1} kpc from the center of the cluster. A Gaussian fit to the data is overlaid.

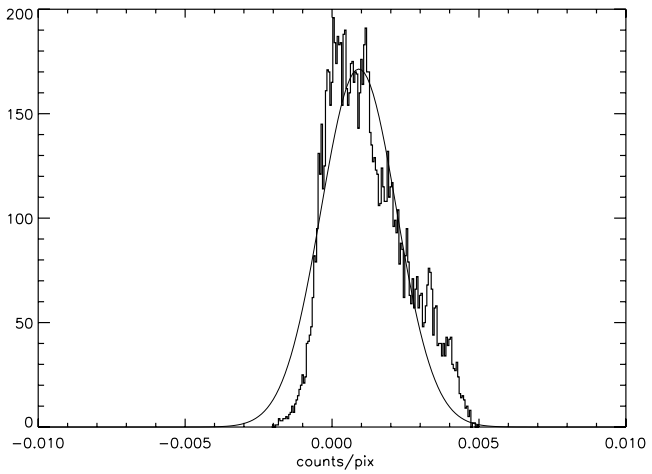

FIG. 13.—Same as Fig. 12, but in the *r* band.

contributions from the bias and dark subtraction, physical variations in the sky level, and the statistical uncertainties mentioned above.

This empirical measurement of the large-scale background fluctuations is likely to be a worst-case estimate of the accuracy with which we can measure surface brightness on large scales because it is derived from the outer regions of the image, where only 6–10 individual exposures have been combined. In the central regions of our imaging ($r < 800\,h_{70}^{-1}$ kpc), roughly twice as many dithered images have been combined, which has the effect of smoothing out large-scale fluctuations in the illumination pattern to a greater degree. We therefore expect greater accuracy in the center of the image where the ICL is being measured.

All sources of uncertainty are listed in Table 3. In addition to the dominant uncertainty from the measurement of the large-scale fluctuations on the background as discussed above, we quantify the contributions from the photometry, masking, and the accuracy with which we can measure the mean in the individual elliptical isophotes. In total the error on the ICL flux is 26% in *V* and 33% in *r*, which in addition to a 16% error in the total cluster flux leads to a 30%–40% uncertainty in the fractional flux.

8. DISCUSSION

We measure a diffuse intracluster component in A3888 to a radius of $\sim$700 h_{70}^{-1} kpc in the *V* and *r* bands down to 28.9 and 28.2 mag arcsec^{-2}, respectively. We discuss here the physical implications of the color, total flux, and profile shape of the ICL.

8.1. *Color Implications*

Color information can place constraints on the age and metallicity of the progenitor population of the ICL, thereby shedding light on the dominant physical mechanisms and timescales for galaxy disruption. Color information may also be able to differentiate between the morphological types of progenitor galaxies.

The color of the ICL in A3888 is consistent with some previous observational results in other clusters, although those results vary widely. Schombert (1988) and Mackie (1992) have found a wide range of results for cD envelopes, from blue to red, with and without color gradients. These surveys have typically been sensitive to a diffuse component within 100–150 h_{70}^{-1} kpc, a much smaller radial extent than this survey. Recently, Gonzalez et al. (2000) have found a mild color gradient where the ICL becomes redder with radius by $W - I = 0.25 \pm 0.08$ from 10 to 70 h_{70}^{-1}kpc. Again, our observations cover a much larger radial region of A3888, and we have no information on the ICL in the core region because it contains several complicated, unmerged clumps. Over a range in radius similar to that for our measurement, Zibetti et al. (2005), from a stack of hundreds of Sloan Digital Sky Survey (SDSS) clusters, find an ICL including the BCG that is similar in color to the galaxy light and has a flat or slightly blue color gradient with radius.

If the ICL is composed of stars stripped from galaxies, its color relative to the galaxies is indicative of the epoch when it was stripped in the following sense. If the ICL is redder than the cluster galaxies, it is likely to have been stripped from the galaxies at early times (higher *z*). Stripped stars will passively evolve toward red colors, while the galaxies will continue to form stars. If, on the other hand, the ICL is of similar color to the average galaxy, the ICL is likely to have formed from the ongoing stripping of stars (via harassment as in Moore et al. 1996). In this case the stripped stars should have roughly the same color at the current epoch as the galaxies at the current epoch. This picture is complicated by the fact that clusters are not made up of galaxies that were all formed at a single epoch, and in addition, we do not know the star formation rates of galaxies once they enter a cluster. While these simple trends hold for the colors of intracluster stars compared to galaxies, the color difference between

TABLE 3
ERROR BUDGET

			Contribution to ICL Uncertainty (%)					
	1 σ Uncertainty		$\mu(0''$–$100'')$		$\mu(100''$–$200'')$		Total ICL Flux	
Source	(*V*)	(*r*)	(*V*)	(*r*)	(*V*)	(*r*)	(*V*)	(*r*)
Background level[a]	29.5 (mag arcsec^{-2})	28.8 (mag arcsec^{-2})	14	18	39	45	24	31
Photometry	0.02 (mag)	0.03 (mag)	2	3	2	3	2	3
Masking[b]	Variation in mask area $\pm$ 30	Variation in mask area $\pm$ 30	5	5	14	19	9	12
Standard deviation in mean[c]	32.7 (mag arcsec^{-2})	32.7 (mag arcsec^{-2})	3	2	2	1	3	1
Total	...	...	15	19	41	50	26	33
Cluster flux[d]	16%	16%	...	...	...	...	...	...

[a] Large-scale fluctuations in background level are measured empirically and include instrumental calibration uncertainties, as well as true variations in background level (see § 7).
[b] Object masks were scaled by $\pm$30% in area to test the impact on ICL measurement (see § 5.2.2).
[c] The statistical uncertainty in the mean surface brightness of the ICL in each isophote.
[d] Errors on the total cluster flux are based on errors in the fit to the luminosity function (see § 5.3).

passively evolving stars and low–star formation galaxies may not be large enough to detect.

Cluster evolution is complex due to a myriad of environmental influences. Several groups have produced hierarchical, ΛCDM simulations of clusters that include radiative cooling, star formation, and various feedback mechanisms but differ primarily in star formation prescriptions and numerical resolution. These models can be divided based on their broad, empirical predictions for the color/formation epoch of the ICL.

Theoretical models in which the ICL forms early in the cluster history all suggest an ICL that is older and redder than the galaxy population because the galaxies continue to form new stars and therefore have younger mean ages than the ICL population (Dubinski 1998; Murante et al. 2004; Sommer-Larsen et al. 2005). This is generally consistent with our results in the outer regions of A3888. Specifically, Sommer-Larsen et al. (2005) predict a slight color gradient in $B - R$ such that the ICL becomes 0.1 mag bluer from 0 to 600 h_{70}^{-1} kpc, while our data suggest the opposite trend with radius in $V - r$.

Theoretical models in which the ICL forms throughout the cluster lifetime generally predict a younger, bluer ICSP (Willman et al. 2004; Moore et al. 1999; Gnedin 2003; Bekki et al. 2001), since more recent stripping will have the chance to pull newly formed stars out of galaxies. Ongoing stripping is consistent with our results within about 400 h_{70}^{-1} kpc, where the ICL is roughly the same color or slightly bluer than the red cluster sequence. In an N-body + smoothed particle hydrodynamics simulation, Willman et al. (2004) find that 50% of intracluster stars come from M_* or brighter galaxies, which means the color of the intracluster stars should be in accord with the color of the outskirts of bright cluster galaxies or equivalently the color of intermediate-luminosity galaxies. The intermediate-luminosity galaxies that we consider members of A3888 have a color in the range $V - r = 0.1$–0.4. Our results are consistent with this prediction in the inner regions of the cluster.

Recent observations of some intracluster H II regions (such as those found in Virgo by Gerhard et al. [2002], Ryan-Weber et al. [2004], and Cortese et al. [2004]) indicate that it may be possible for some intracluster stars to form in situ. In this case, the ICL color will still depend on the formation epoch. If the ICSP is just now forming in intracluster H II regions, then it will be blue; however, if it formed earlier in cluster formation, then the ICSP will passively evolve toward redder colors. Only if the ICL were significantly bluer than the existing cluster galaxies could it be possible to definitively state from the color that a significant fraction of the ICL formed in situ. Since this is not the case in A3888, our results cannot constrain the formation site of the ICL.

Using N-body simulations, both Moore et al. (1999) and Gnedin (2003) find that low-density galaxies (LSB and dwarf galaxies) are the main contributers to the ICL. Low surface brightness galaxies in SDSS data have a color range of $B - V = 0.4$–1.3 (Kniazev et al. 2004), which corresponds to $V - r = -0.2$–0.7. Dwarf galaxies in Coma have $V - r \simeq 0.5 \pm 0.3$ (Trentham 1998). This range is sufficiently broad that it is consistent with the ICL at all radii in A3888, implying that the ICL could have origins in LSB or dwarf galaxies.

In summary, the ICL in the outer regions of A3888 is consistent with predictions for a stellar population that formed at redshifts higher than 1 and is significantly metal-rich, implying an ICL that forms early with the collapse of the main cluster. The ICL in the center of A3888 ($r < 400\ h_{70}^{-1}$ kpc) is consistent with predictions for a relatively younger population. This implies that within some core radius harassment-type interactions are the dominant mechanism.

8.2. *Fractional Flux Implications*

Another clue to the dominant mechanism driving evolution in clusters comes from correlating ICL properties with the properties of the parent cluster. For example, a trend in ICL fraction with cluster mass but not redshift, richness, or morphology would indicate that mass was the dominant mechanism that could predict ICL fraction. The calculation of the fractional ICL flux depends on many observational parameters, including the surface brightness and radial limit of the ICL measurement itself, the surface brightness at which individually bound, resolved sources are distinguished from the ICL, and the volume over which the ICL flux and galaxy flux are measured. As these parameters vary widely in work by previous groups, it is difficult to make meaningful comparisons with results for other clusters in the literature. In addition, A3888 is a very massive cluster and is not as simple as clusters with a cD or clear BCG. A1914 is the only cluster with an ICL measurement (Feldmeier et al. 2004) that has overall similar characteristics to A3888. With similar detection limits to those employed here, those authors find an ICL fraction of 7% in the V band, which is generally consistent with our results for A3888.

With these observational complications and cluster parameters in mind, we can only generally conclude that previous measurements of the ICL in clusters over a wide range in redshift ($0.003 < z < 0.41$) and mass [$(1$–$35) \times 10^{14}\ M_\odot$] are roughly 10%. There are no obvious trends with mass or redshift, although there are some noteworthy outliers at 50% for Coma (Bernstein et al. 1995) and 0% for A1689 (Gudehus 1989). The Bernstein et al. (1995) result covers a small radial extent and is therefore biased toward higher fractional flux values. It is difficult to interpret the Gudehus (1989) measurement due to disparate methods. There is some evidence that the ICL fraction is dependent on cluster morphology; B/M type I clusters (Theuns & Warren 1997; Feldmeier et al. 2002; Uson et al. 1991; Vilchez-Gomez et al. 1994) have a reported average ICL fraction marginally higher than those with B/M type III (Vilchez-Gomez et al. 1994; Feldmeier et al. 2004; Arnaboldi et al. 2003; Ferguson et al. 1998; Durrell et al. 2002). However, poor morphological classification, small number statistics, and widely disparate methods and accuracies among the different measurements make any possible trends difficult to quantify.

In comparing the observed ICL with simulations, it is important to note that the simulations generally report the fractional light in the ICL out to much larger radii (e.g., r_{200}) than its surface brightness can be measured observationally. At smaller radii, the predicted ratio of ICL to galaxy light would be larger. Bearing this in mind, Willman et al. (2004) find a lower limit for fractional flux in the ICL of 10%–22% at r_{200} for a Virgo-like cluster from $z = 1.1$ to 0 (increasing fractional flux with time). At the maximum radius of our ICL measurement ($\sim 0.3 r_{200}$), the fraction would presumably be higher by at least a factor of 2, making it larger than we observe in A3888. Other predictions are similarly high. For a cluster with the mass of A3888 ($25 \times 10^{14}\ h_{70}^{-1}\ M_\odot$), both Lin & Mohr (2004) and Murante et al. (2004) predict an ICL fraction in excess of 40%. To be consistent with their predictions, this cluster would require a factor of greater than 100 lower mass to have only 10% ICL, and although this cluster is not dynamically relaxed, such large errors in mass are not realistic.

In summary, we find an ICL fraction that is roughly compatible with observed ICL measurements in other clusters.

However, our measurement differs significantly from theoretical estimates, particularly considering A3888's large total mass. The dynamical state of A3888 may contribute to this discrepancy, as morphology may have a significant influence over ICL fraction. We emphasize again that A3888 is not a relaxed cluster; it does not have a cD galaxy and its X-ray isophotes are not circular. If we have caught this cluster as it is just now entering its major merger phase, we would expect a low ICL fraction as compared with a cluster at this redshift, mass, and richness that had already reached dynamic equilibrium. In contrast, when examining Coma, a cluster with an extremely high ICL fraction but lower mass, we note that its morphology indicates that it has already undergone significant merging to produce two cD-like galaxies. If morphology is the dominant influence on ICL flux, we should find A3888 to have a similar ICL fraction to other clusters with similar morphologies. Comparable measurements of the ICL in our remaining sample will help resolve this issue.

8.3. *Profile Shape Implications*

As discussed in § 6.1, the profile of the ICL is generally stepper at smaller radii. In particular, the steepening profile near the core region of the cluster is associated with the three apparently merging groups of galaxies in the center of the cluster. The recent interactions in the center have likely added and continue to add ICL, which is likely to eventually relax into a BCG and BCG halo. The profile in the outer region of the cluster is consistent with previous measurements of BCG envelopes that follow shallower profiles (Gonzalez et al. 2005). In addition, Bernstein et al. (1995) and Zibetti et al. (2005) find a steeper profile for the Coma cluster and for a stacked profile of hundreds of SDSS clusters. This steeper profile is consistent with some theoretical predictions, particularly by Murante et al. (2004) based on a hydrodynamic simulation including radiative cooling, star formation, and SN feedback.

9. CONCLUSION

We have presented results for the first of 10 clusters in our sample. We have identified an intracluster component in A3888 to $\sim$700 h_{70}^{-1} kpc from the center of the cluster down to 28.9 mag arcsec^{-2} in the V band and 28.2 mag arcsec^{-2} in the Gunn-r band. This ICL component is aligned with the hot gas in the cluster, which is evidence of its correlation with the underlying mass distribution. There is a second diffuse component around a group of galaxies 1.4 h_{70}^{-1} Mpc from the center of the cluster, which is consistent with preprocessing in an infalling group. In addition to these two diffuse ICL components, we find three LSB features consistent with being remnants from tidal interactions.

Beyond 400 h_{70}^{-1} kpc from the center of the cluster, the ICL is redder than the galaxies, implying an older population of stars. Inside of 400 h_{70}^{-1} kpc the ICL has a similar color to the galaxies. We interpret this color gradient in the ICL ($V - r = 0.3$–0.7, from inner to outer) as evidence of younger intracluster stars in the center of the cluster. Consequently, we suggest that more than one process is likely stripping stars from cluster galaxies. Specifically, harassment-type interactions are still ongoing in the center of the cluster, while galaxy mergers may have played a significant role earlier in the history of the cluster.

We find that the ICL component in A3888 does not follow the same light profile as the resolved sources but has a smoother and slightly steeper profile than the galaxies. Due to a steepening profile within 400 h_{70}^{-1} kpc, the ICL profile can be described by a double exponential function. A double profile is consistent with ongoing dynamical activity in the center of this cluster producing a new population of intracluster stars.

Comparing the ICL to cluster galaxy flux, we find that the ICL component in A3888 accounts for roughly 13% of the total cluster flux within 700 h_{70}^{-1} kpc ($\sim 0.3 r_{200}$). This value is low compared to the theoretical predictions for a cluster of this mass and may be partly due to the fact that A3888 appears to be a dynamically young cluster. The ICL in A3888 will likely increase with time due to contributions from an infalling group, as well as through major mergers in the center to create a cD galaxy.

We acknowledge C. Peng and L. Simard for help with their galaxy profile fitting algorithms. We thank the anonymous referee for useful suggestions on the manuscript. Partial support for J. E. K. was provided by the National Science Foundation (NSF) through the University of Michigan's NSF ADVANCE program. Partial support for R. A. B. was provided by NASA Hubble Fellowship grant HF-01088.01-97A awarded by the Space Telescope Science Institute, which is operated by the Association of Universities for Research in Astronomy, Inc., for NASA under contract NAS5-2655. This research has made use of data from the following sources: the USNOFS Image and Catalogue Archive operated by the US Naval Observatory, Flagstaff Station (http://www.nofs.navy.mil/data/fchpix); the NASA/IPAC Extragalactic Database, which is operated by the Jet Propulsion Laboratory, California Institute of Technology, under contract with the National Aeronautics and Space Administration; the Two Micron All Sky Survey, which is a joint project of the University of Massachusetts and the Infrared Processing and Analysis Center/California Institute of Technology, funded by the National Aeronautics and Space Administration and the NSF; and the SIMBAD database, operated at CDS, Strasbourg, France.

REFERENCES

Abell, G. O., Corwin, H. G., & Olowin, R. P. 1989, ApJS, 70, 1
Aguerri, J. A. L., Gerhard, O. E., Arnaboldi, M., Napolitano, N. R., Castro-Rodriguez, N., & Freeman, K. C. 2005, AJ, 129, 2585
Allen, S. W., Schmidt, R. W., Ebeling, H., Fabian, A. C., & van Speybroeck, L. 2004, MNRAS, 353, 457
Arnaboldi, M., Gerhard, O., Aguerri, J. A. L., Freeman, K. C., Napolitano, N. R., Okamura, S., & Yasuda, N. 2004, ApJ, 614, L33
Arnaboldi, M., et al. 2003, AJ, 125, 514
Bassino, L. P., Cellone, S. A., Forte, J. C., & Dirsch, B. 2003, A&A, 399, 489
Batuski, D. J., Miller, C. J., Slinglend, K. A., Balkowski, C., Maurogordato, S., Cayatte, V., Felenbok, P., & Olowin, R. 1999, ApJ, 520, 491
Beers, T. C., Flynn, K., & Gebhardt, K. 1990, AJ, 100, 32
Bekki, K., Couch, W. J., & Drinkwater, M. J. 2001, ApJ, 552, L105
Bernstein, G. M., Nichol, R. C., Tyson, J. A., Ulmer, M. P., & Wittman, D. 1995, AJ, 110, 1507
Bertin, E., & Arnouts, S. 1996, A&AS, 117, 393
Broadhurst, T. J., Taylor, A. N., & Peacock, J. A. 1995, ApJ, 438, 49
Bruzual, G., & Charlot, S. 2003, MNRAS, 344, 1000
Busarello, G., Merluzzi, P., La Barbera, F., Massarotti, M., & Capaccioli, M. 2002, A&A, 389, 787
Calcáneo-Roldán, C., Moore, B., Bland-Hawthorn, J., Malin, D., & Sadler, E. M. 2000, MNRAS, 314, 324
Castro-Rodríguez, N., Aguerri, J. A. L., Arnaboldi, M., Gerhard, O., Freeman, K. C., Napolitano, N. R., & Capaccioli, M. 2003, A&A, 405, 803
Chen, J., Huchra, J. P., McNamara, B. R., & Mader, J. 1998, BAAS, 30, 1307
Ciardullo, R., Ford, H., & Harms, R. 1985, ApJ, 293, 69
Collins, C. A., Guzzo, L., Nichol, R. C., & Lumsden, S. L. 1995, MNRAS, 274, 1071
Cortese, L., Gavazzi, G., Boselli, A., & Iglesias-Paramo, J. 2004, A&A, 416, 119

Couch, W. J., Balogh, M. L., Bower, R. G., Smail, I., Glazebrook, K., & Taylor, M. 2001, ApJ, 549, 820
Couch, W. J., & Newell, E. B. 1984, ApJS, 56, 143
Couch, W. J., & Sharples, R. M. 1987, MNRAS, 229, 423
Dahle, H., Kaiser, N., Irgens, R. J., Lilje, P. B., & Maddox, S. J. 2002, ApJS, 139, 313
Dalcanton, J. J., Spergel, D. N., Gunn, J. E., Schmidt, M., & Schneider, D. P. 1997, AJ, 114, 635
De Filippis, E., Bautz, M. W., Sereno, M., & Garmire, G. P. 2004, ApJ, 611, 164
den Hartog, R. 1995, Ph.D. thesis, Univ. Leiden
De Propris, R., et al. 2002, MNRAS, 329, 87
Domainko, W., Gitti, M., Schindler, S., & Kapferer, W. 2004, A&A, 425, L21
Driver, S. P., Couch, W. J., & Phillipps, S. 1998, MNRAS, 301, 369
Dubinski, J. 1998, ApJ, 502, 141
Durrell, P. R., Ciardullo, R., Feldmeier, J. J., Jacoby, G. H., & Sigurdsson, S. 2002, ApJ, 570, 119
Durrell, P. R., Decesar, M. E., Ciardullo, R., Hurley-Keller, D., & Feldmeier, J. J. 2004, in IAU Symp. 217, Recycling Intergalactic and Interstellar Matter, ed. P.-A. Duc, J. Braine, & E. Brinks (San Francisco: ASP), 90
Ebeling, H., Voges, W., Bohringer, H., Edge, A. C., Huchra, J. P., & Briel, U. G. 1996, MNRAS, 281, 799
Feldmeier, J. J., Mihos, J. C., Morrison, H. L., Harding, P., Kaib, N., & Dubinski, J. 2004, ApJ, 609, 617
Feldmeier, J. J., Mihos, J. C., Morrison, H. L., Rodney, S. A., & Harding, P. 2002, ApJ, 575, 779
Ferguson, H. C., Tanvir, N. R., & von Hippel, T. 1998, Nature, 391, 461
Fujita, Y. 2004, PASJ, 56, 29
Fukugita, M., Shimasaku, K., & Ichikawa, T. 1995, PASP, 107, 945
Gerhard, O., Arnaboldi, M., Freeman, K. C., Kashikawa, N., Okamura, S., & Yasuda, N. 2005, ApJ, 621, L93
Gerhard, O., Arnaboldi, M., Freeman, K. C., & Okamura, S. 2002, ApJ, 580, L121
Girardi, M., Borgani, S., Giuricin, G., Mardirossian, F., & Mezzetti, M. 1998, ApJ, 506, 45
Girardi, L., Bressan, A., Chiosi, C., Bertelli, G., & Nasi, E. 1996, A&AS, 117, 113
Girardi, M., Escalera, E., Fadda, D., Giuricin, G., Mardirossian, F., & Mezzetti, M. 1997, ApJ, 482, 41
Girardi, M., & Mezzetti, M. 2001, ApJ, 548, 79
Gnedin, O. Y. 2003, ApJ, 589, 752
Gonzalez, A. H., Zabludoff, A. I., & Zaritsky, D. 2005, ApJ, 618, 195
Gonzalez, A. H., Zabludoff, A. I., Zaritsky, D., & Dalcanton, J. J. 2000, ApJ, 536, 561
Gregg, M. D., & West, M. J. 1998, Nature, 396, 549
Gudehus, D. H. 1989, ApJ, 340, 661
Hilker, M. 2003, in Extragalactic Globular Cluster Systems, ed. M. Kissler-Patig (Berlin: Springer), 173
Jedrzejewski, R. I. 1987, MNRAS, 226, 747
Jordán, A., West, M. J., Côté, P., & Marzke, R. O. 2003, AJ, 125, 1642
Jorgensen, I. 1994, PASP, 106, 967
Kelson, D. D., Zabludoff, A. I., Williams, K. A., Trager, S. C., Mulchaey, J. S., & Bolte, M. 2002, ApJ, 576, 720
Kniazev, A. Y., Grebel, E. K., Pustilnik, S. A., Pramskij, A. G., Kniazeva, T. F., Prada, F., & Harbeck, D. 2004, AJ, 127, 704
Kowalski, M. P., Ulmer, M. P., & Cruddace, R. G. 1983, ApJ, 268, 540
Landolt, A. U. 1992, AJ, 104, 340
Leinert, C., et al. 1998, A&AS, 127, 1
Lin, Y., & Mohr, J. J. 2004, ApJ, 617, 879
Mackie, G. 1992, ApJ, 400, 65
Marín-Franch, A., & Aparicio, A. 2003, ApJ, 585, 714
Markevitch, M. 1998, ApJ, 504, 27
Mazure, A., et al. 1996, A&A, 310, 31
Moore, B., Katz, N., Lake, G., Dressler, A., & Oemler, A. 1996, Nature, 379, 613
Moore, B., Lake, G., Stadel, J., & Quinn, T. 1999, in ASP Conf. Ser. 170, The Low Surface Brightness Universe, ed. J. I. Davies, C. Impey, & S. Phillipps (San Francisco: ASP), 229
Murante, G., et al. 2004, ApJ, 607, L83
O'Neil, K., Bothun, G. D., & Cornell, M. E. 1997, AJ, 113, 1212
Peng, C. Y., Ho, L. C., Impey, C. D., & Rix, H. 2002, AJ, 124, 266
Pimbblet, K. A., Smail, I., Kodama, T., Couch, W. J., Edge, A. C., Zabludoff, A. I., & O'Hely, E. 2002, MNRAS, 331, 333
Reimers, D., Koehler, T., & Wisotzki, L. 1996, A&AS, 115, 235
Reiprich, T. H., & Böhringer, H. 2002, ApJ, 567, 716
Ryan-Weber, E. V., et al. 2004, AJ, 127, 1431
Schombert, J. M. 1988, ApJ, 328, 475
Simard, L., et al. 2002, ApJS, 142, 1
Smail, I., Ellis, R. S., Fitchett, M. J., Norgaard-Nielsen, H. U., Hansen, L., & Jorgensen, H. E. 1991, MNRAS, 252, 19
Sommer-Larsen, J., Romeo, A. D., & Portinari, L. 2005, MNRAS, 357, 478
Stein, P. 1996, A&AS, 116, 203
Struble, M. F., & Ftaclas, C. 1994, AJ, 108, 1
Struble, M. F., & Rood, H. J. 1999, ApJS, 125, 35
Teague, P. F., Carter, D., & Gray, P. M. 1990, ApJS, 72, 715
Theuns, T., & Warren, S. J. 1997, MNRAS, 284, L11
Trentham, N. 1998, MNRAS, 293, 71
Trujillo, I., Aguerri, J. A. L., Gutiérrez, C. M., & Cepa, J. 2001, AJ, 122, 38
Uson, J. M., Boughn, S. P., & Kuhn, J. R. 1991, ApJ, 369, 46
Vilchez-Gomez, R., Pello, R., & Sanahuja, B. 1994, A&A, 283, 37
Willman, B., Governato, F., Wadsley, J., & Quinn, T. 2004, MNRAS, 355, 159
Wu, X., Xue, Y., & Fang, L. 1999, ApJ, 524, 22
Zaritsky, D., Gonzalez, A. H., & Zabludoff, A. I. 2004, ApJ, 613, L93
Zibetti, S., White, S. D. M., Schneider, D. P., & Brinkmann, J. 2005, MNRAS, 358, 949